350
1-8-81
JWL

(2)

Dr. 2202
COO-3056-45

ELECTRON REFLECTION FROM ONE-DIMENSIONAL POTENTIAL BARRIERS

Topical Report

MASTER

D154-285
NTIS-25

By
C. L. Balestra
F. N. Huffman
C. C. Wang

September 1978

Work Performed Under Contract No. AC02-76ET11293

Thermo Electron Corporation
Waltham, Massachusetts

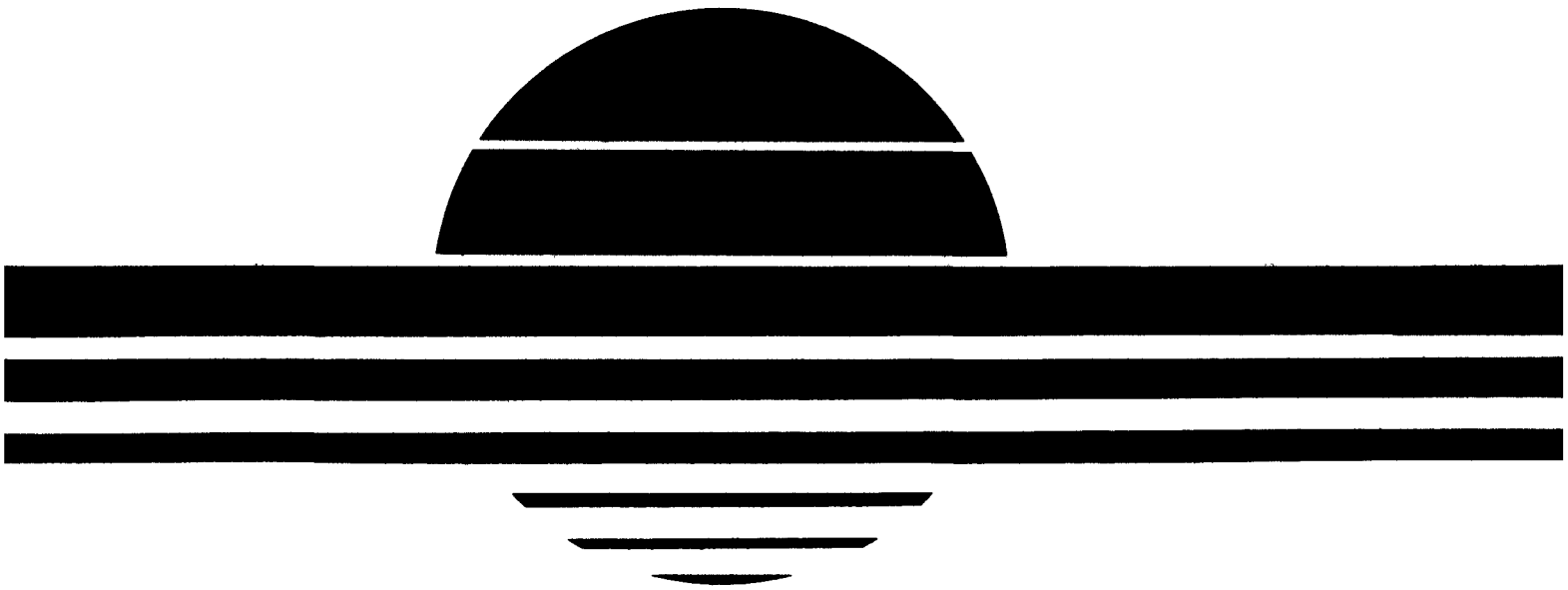

U.S. Department of Energy

Solar Energy

DISCLAIMER

DISCLAIMER

Available from the National Technical Information Service, U. S. Department of Commerce, Springfield, Virginia 22161.

Price: Paper Copy $7.00
Microfiche $3.50

COO-3056-45
Distribution Category UC-59c

Report No. TE4237-38-79

TOPICAL REPORT
ELECTRON REFLECTION FROM ONE-DIMENSIONAL POTENTIAL BARRIERS

By
C.L. Balestra, F.N. Huffman, and C.C. Wang

September 1978

Prepared for

U.S. Department of Energy
Contract No. EY-76-C-02-3056

Prepared by

Thermo Electron Corporation
85 First Avenue
Waltham, Massachusetts 02154

BLANK

TABLE OF CONTENTS

BLANK

GLOSSARY OF SYMBOLS

A, A_k B C D G	:	Constant Coefficients
$Ai(z)$ $Bi(z)$	:	Airy Functions
E	:	Total electron energy (eV)
$I_n(Z)$ $K_n(Z)$	:	Modified Bessel Functions
$M(a, b, z)$	:	Confluent hypergeometric function of first kind
$R(E)$	:	Electron reflectivity, reflection coefficient
$U(a, b, z)$	:	Confluent hypergeometric function of second kind
$V(x)$	:	Potential energy function (eV)
b	:	Surface barrier thickness (angstroms)
e	:	Electron charge (-1.602 Coulombs)
$f_+(x), f_-(x)$	:	General electron wave functions
h_1, h_2	:	Constant coefficients
$\hbar$	:	Planck's constant divided by 2 (1.0546 Joule-seconds)
$\Gamma(z)$	:	Gamma function
γ	:	Euler's constant (0.5772)
ϵ_o	:	Permittivity of free space (8.854×10^{-12} Farads/meter)
μ	:	Fermi level relative to zero kinetic energy (eV)
$\psi_{(x)}$	:	Digamma Function

$\phi(x)$	:	Electron wave function
ϕ_b	:	Surface barrier height (eV)
ϕ_e	:	Work function (eV)
ζ	:	Effective heat transport factor
m	:	Electron mass (0.91095×10^{-30} kg)
k	:	Boltzmann's constant (1.3806×10^{-23} jk)$^{-1}$
H	:	Slope (eV/Å) of triangular barrier

I. INTRODUCTION

A low collector work function is essential for efficient thermionic energy conversion (TEC). Accordingly, a substantial portion of Thermo Electron's TEC effort is directed toward a minimization of collector work function within the constraints of converter operating conditions. However, as progress has been made in improving TEC performance along this avenue several anomalous results (discussed in Section II) have become apparent. These results, coupled with field emission retarding potential (FERP) measurements suggest that electron reflectivity of the collector may be an important mechanism in TEC. These data also imply the possibility of using electron reflectivity to an advantage by selectively returning the hotter electrons to the plasma in order to reduce the arc drop loss.

Investigations at Thermo Electron indicate that low work function surfaces formed by cesium-oxygen composites are amorphous and are of the order of 30 Å thick. Since the DeBroglie wavelentgh of a thermal electron is of comparable magnitude, it is not surprising that a strong interaction (i. e., reflection) may occur in a converter between the thermal electrons and a collector covered with a cesium-oxygen composite.

This topical report summarizes the relevant experimental evidence for electron reflectivity effects in TEC and describes the analytical effort to better understand electron reflectivity as a function of the potential configuration of the surface layer. The analyses consider rectangular and triangular barrier models

(described in Section III) with, and without, image potentials. The calculated results are presented in Section IV and discussed in Section V. Details of the solutions are given in Appendices A, B, and C. The computer programs to obtain these results are listed in Appendix D.

These analyses demonstrate that cesium-oxygen composites with potential discontinuties around one volt and 20 Å thick can be expected to be highly reflective to thermal electrons. Consequently, such composites would be expected to have significant effects on TEC performance.

II. EXPERIMENTAL DATA IMPLYING ELECTRON REFLECTIVITY EFFECTS

This section will review the experimental data at Thermo Electron relative to electron reflectivity. First, measurements of electron reflectivity using the field emission retarding potential (FERP) technique will be reviewed. Next, anomalous thermionic converter observations which may be related to electron reflectivity will be discussed.

A. FERP MEASUREMENTS

Direct measurement of the electron collection characteristics have been made using the FERP technique.[1] The underlying principle, as shown in Figure 1, involves the collection of field emission electrons. The threshold of collection is a direct measure of work function in the FERP technique. In contrast, the indirect Kelvin method which determines the contact potential difference between a reference electrode and test electrode, and one can infer the test electrode work function from an assumed value of the reference electrode work function. The Kelvin technique is particularly suspect when working with adsorbates such as cesium which can drastically change the work function of the reference electrode.

In the FERP method, the field emitted electrons are conveyed to the sample surface by means of an electron optics column (depicted in Figure 2) having two Einzel lenses followed by a planar control grid which establishes the appropriate distribution of electrons drawn from the field emitter tip. Their energy, relative to the vacuum level outside the collector, is determined by V_c which can be varied continuously. The energy distribution of these emitted electrons is known.[2]

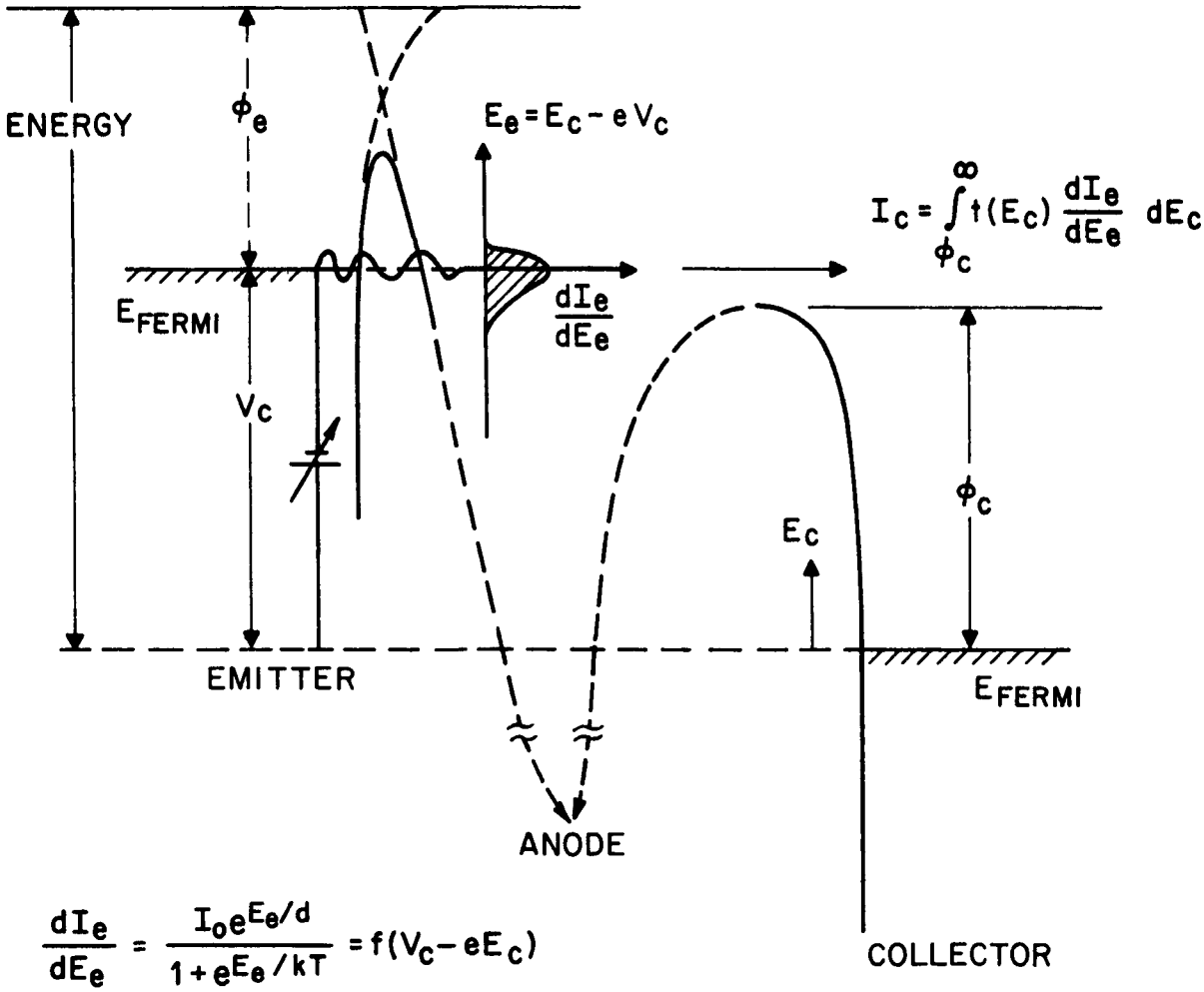

$$\frac{dI_e}{dE_e} = \frac{I_o e^{E_e/d}}{1+e^{E_e/kT}} = f(V_c - eE_c)$$

$$\frac{d^2 I_e}{dE_e^2} = 0, \; E_e = kT \ell n \frac{kT}{d+kT}$$

$$I_c(V_c) = \int_{-\infty}^{\infty} t(E_c) f(V_c - eE_c) dE_c$$

Figure 1. Field Emission Retarding Potential (FERP) Diagram

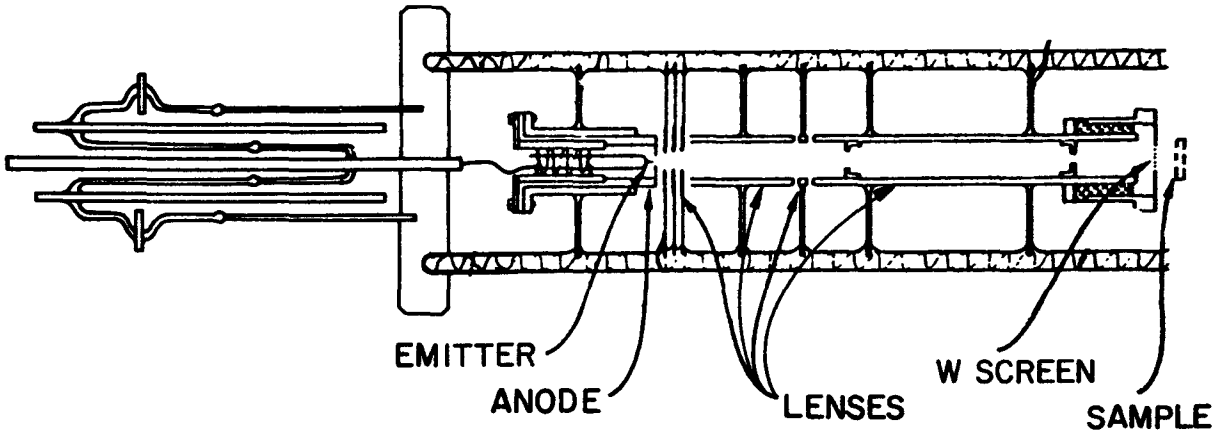

Figure 2. Field Emission Retarding Potential (FERP) Gun.

Although there are distorting effects which are not well established, they can be determined for a particular measurement by means of a Faraday cup. Since the FERP gun is located inside the Surface Characterization Chamber, the chemical composition and composite structure of a sample collector can be correlated with its collector performance.

In the absence of electron reflectivity, the FERP collection curve $I_c(V_c)$, would be zero up to the collection threshold at $V_c = \phi_c$, beyond which I_c would quickly approach a saturation value to be maintained throughout the remainder of the trace. One hundred percent collection is rarely, if ever, observed. Data obtained for a W/Cs/O surface composite on (110) oriented single crystal tungsten is shown in Figure 3. Taking the maximum amplitude of $I_c(V_c)$ to be the saturation value, it is seen that a reflectivity of greater than 50 percent occurs in the electron energy range from 3 to 4 eV. Although obscured by the finite energy distribution of incident electron beam, the reduced amplitude at collection threshold indicates substantial electron reflection for low (thermal) energy electrons as well.

The FERP apparatus is mounted in the Surface Characterization Chamber, shown in Figure 4. This chamber has provisions for cesiating and oxygenating samples. Electron reflectivity data taken with this equipment are shown in Figure 5, for polycrystalline tungsten subjected to an alternating series of exposures to cesium and oxygen. The 1.30 eV composite exhibited significant electron reflectivity at thermal energies and substantially higher reflectivity at electron energies above one eV

The reflection spectra of polycrystalline gallium phosphide exposed to cesium and oxygen are given in Figure 6. These spectra show low electron reflectivities at thermal energies. It is remarkable

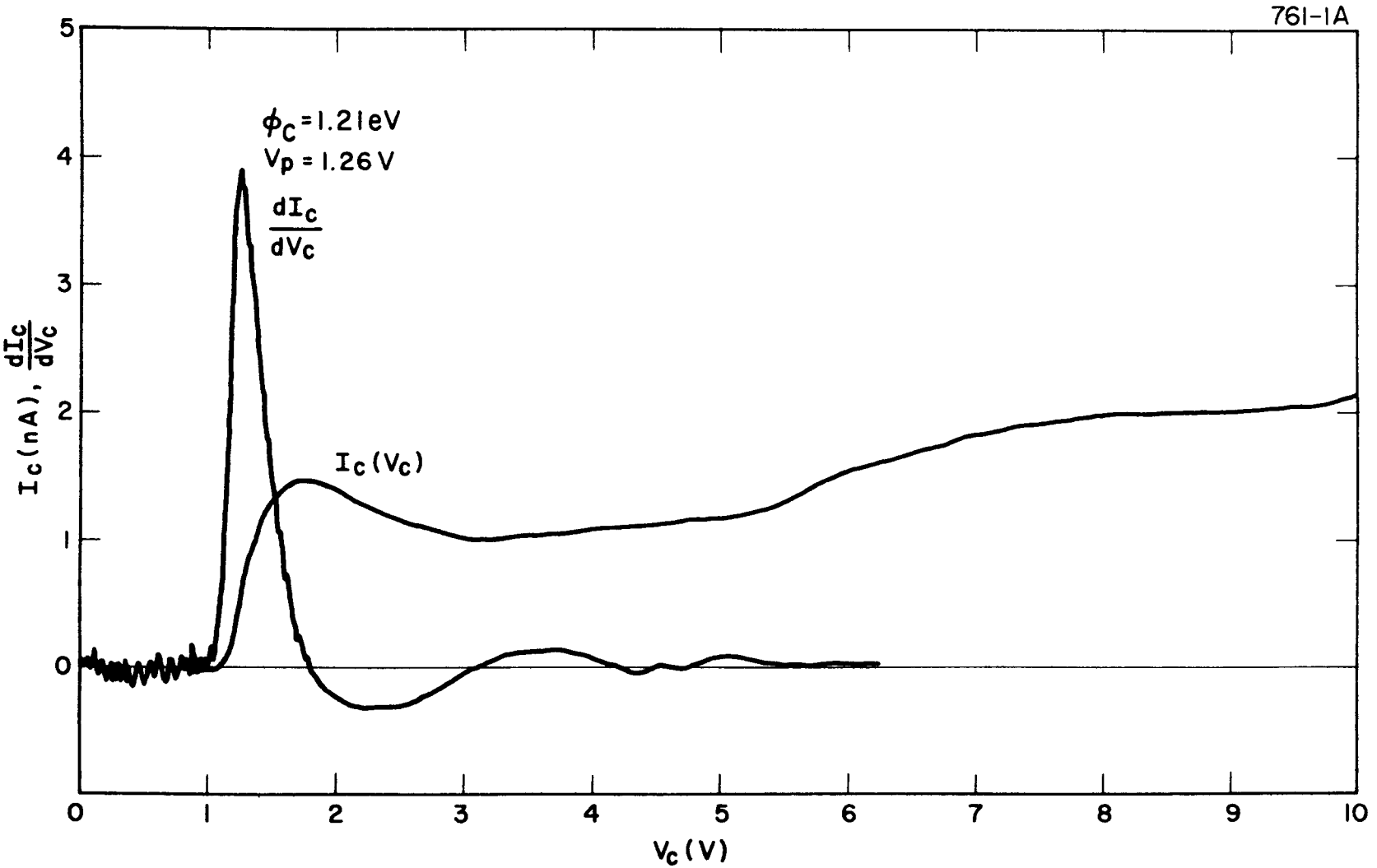

Figure 3. Electron Collection Spectrum of W/C_s/O Surface Composite on a (110) Tungsten Surface.

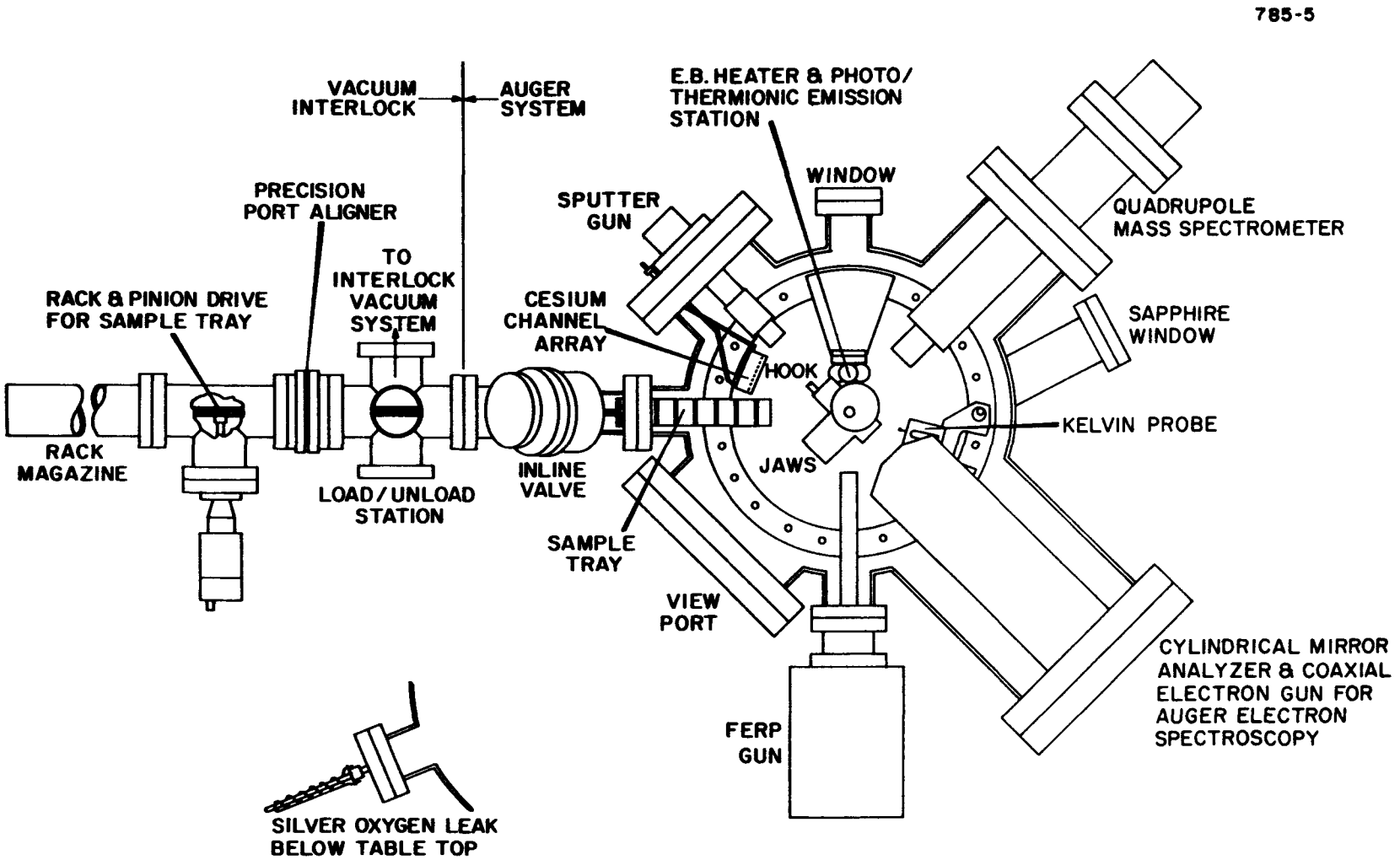

Figure 4. Surface Characterization Chamber

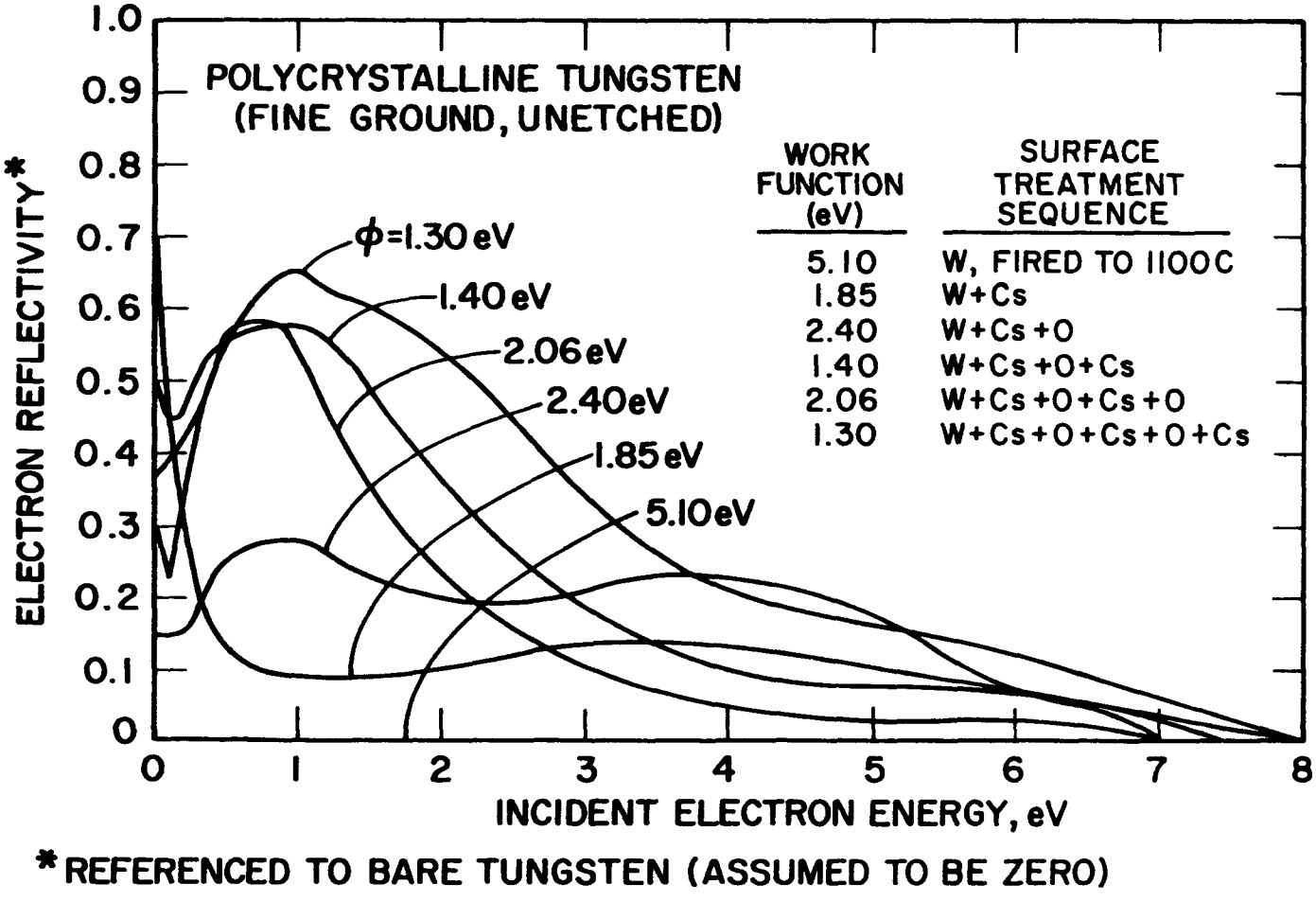

Figure 5. Reflection Spectra of Polycrystalline Tungsten Exposed to Cesium and Oxygen

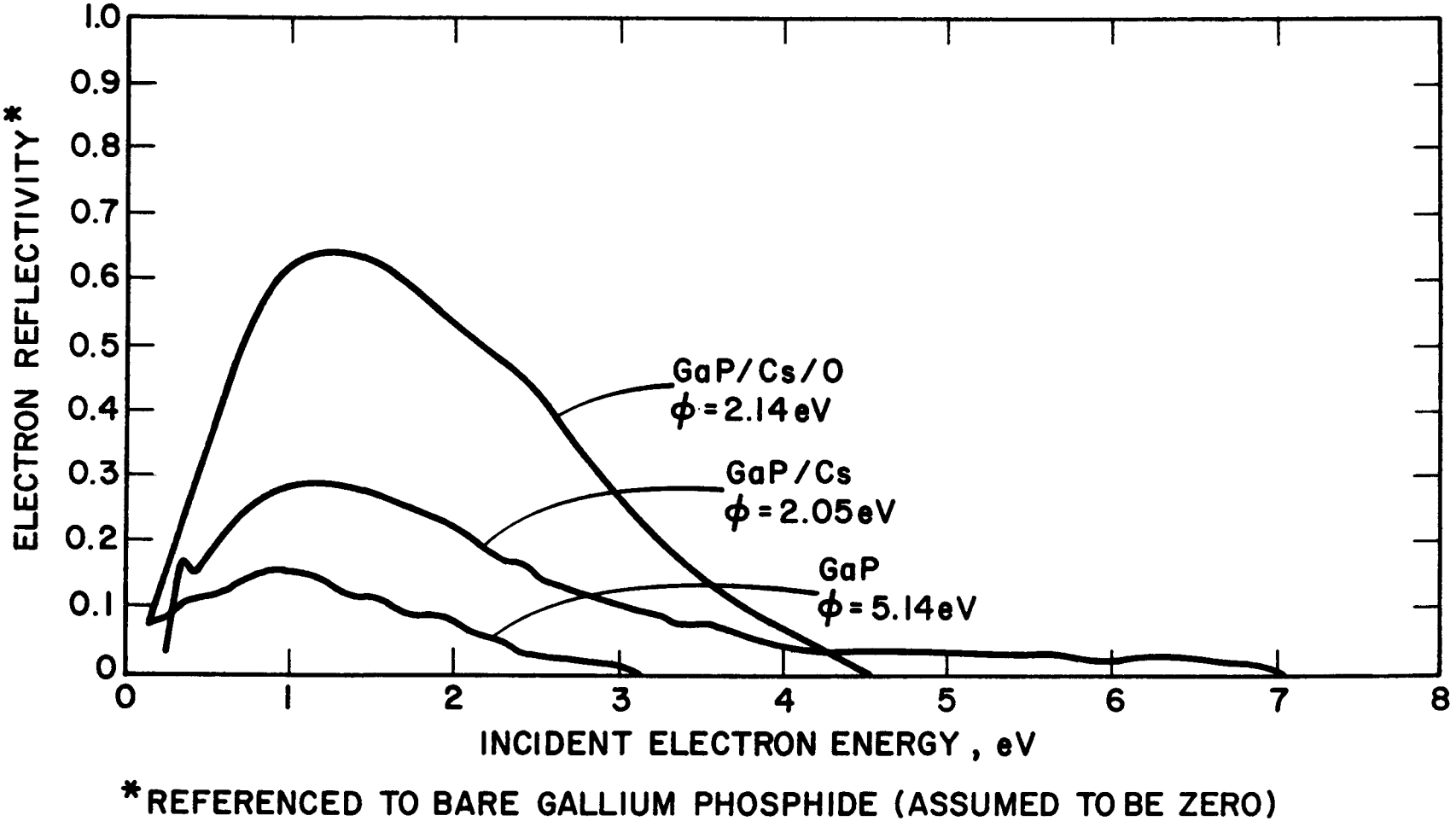

Figure 6. Reflection Spectra of Polycrystalline Gallium Phosphide Exposed to Cesium and Oxygen

that a slight change in work function (i. e., 2. 05 to 2. 14 eV) is associated with a large change in reflectivity in the electron energy range from 0. 5 to 3 eV.

Another set of electron reflectivity spectra are shown in Figure 7 for polycrystalline molybdenum exposed to cesium and oxygen. For this substrate, high electron reflectivity at thermal energies is only evident for the surface with the 1. 87 eV work function.

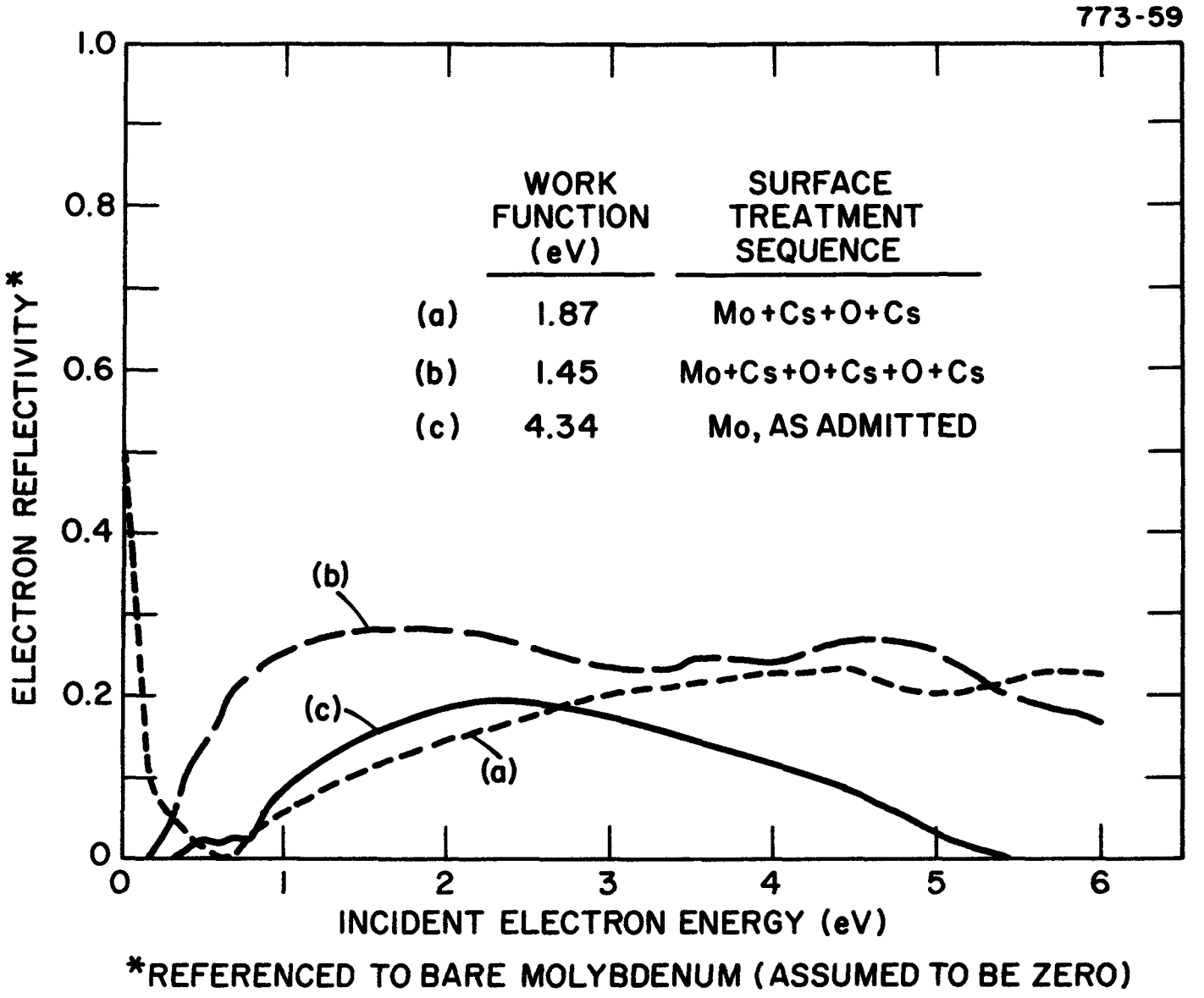

Figure 7. Reflection Spectra of Polycrystalline Molybdenum Exposed to Cesium and Oxygen

B. RUFEH -LIEB ANOMALY

Rufeh and Lieb [3] were the first to note that reductions in collector work function are not fully realized as increases in thermionic converter output voltage - as expected from simple theory. These investigations attempted to correlate variations in collector work function with changes in output voltage and back-emission. The data cover the collector temperature range from 560 to 620 K for inter-electrode spacings of 2.5 to 10 mils.

A comparison of the collector work function (as measured by both back emission and retarding potential methods) and the differential diode output voltage, ΔV is given in Figure 8 versus the ratio of the collector to cesium reservoir temperature. The curves are normalized so that the variations in output voltage coincide with the variations in collector work function at low values of T_C/T_R. The variation in output voltage diverge from the change in collector work function for T_C/T_R values above 1.3.

The discrepancy between expected and measured output voltage takes place at quite low values of thermionic back emission. For example, a difference of 0.1 volt is observed at back emission of 10^{-2} amp as compared to a forward current of 2 amp.

The Rufeh-Lieb anomaly could be explained by electron reflectivity if this parameter increased with decreasing collector work function in a suitable manner. Electron reflectivity at the collector will act as virtual back emission. Such emission could contribute to the formation of a double-valued sheath adjacent to the collector. In the case of a monotonic sheath, the effect of collector reflectivity is to adjust the sheath height to reduce the output voltage for a given current.

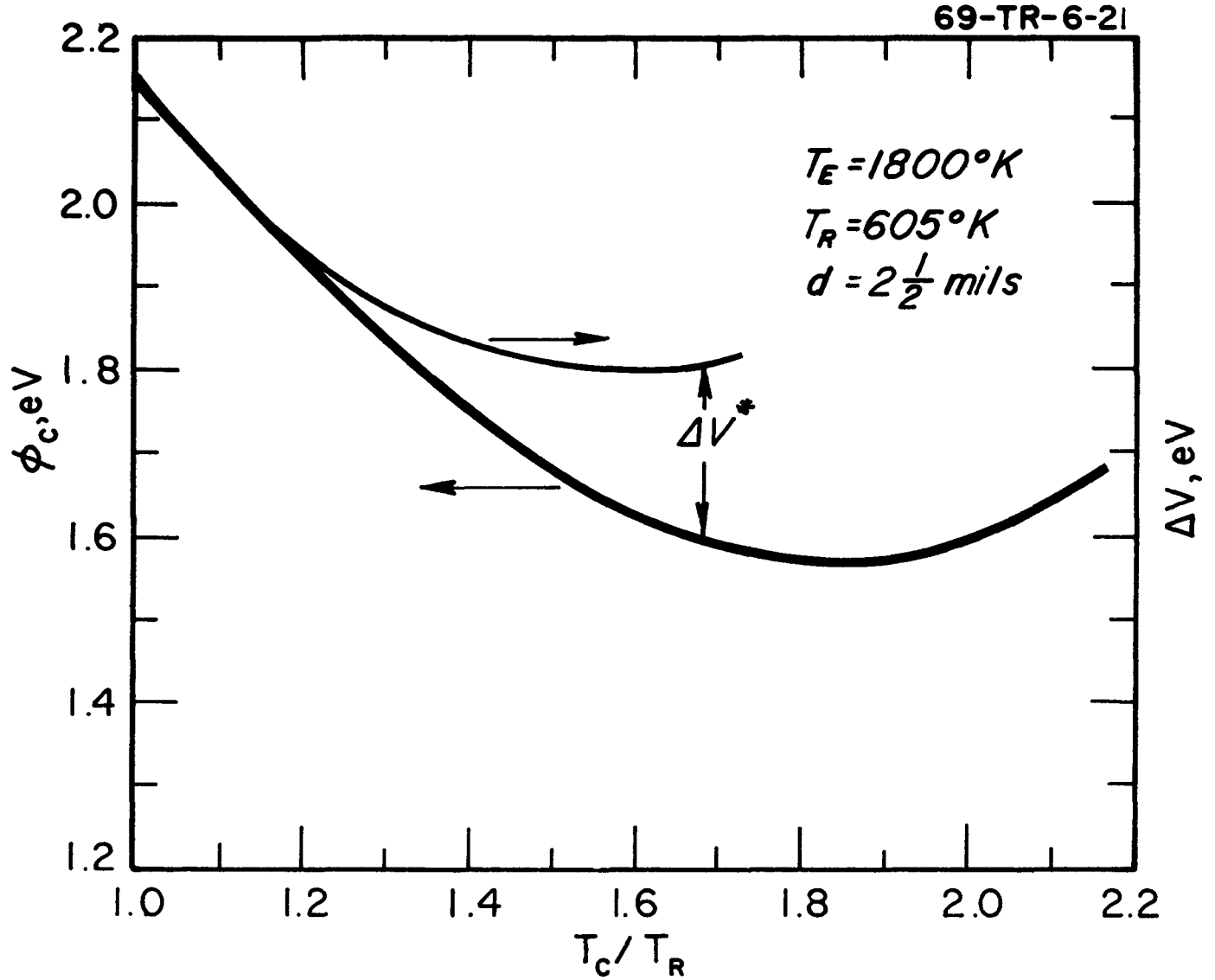

Figure 8. Comparison of Differential Diode Output Voltage and Collector Work Function Versus the Ratio of Collector Temperature to Cesium Reservoir Temperature

However, the preliminary electron reflectivity data obtained on cesiated metals do not show a systematic variation with work function of the proper magnitude. Therefore, a definitive argument cannot be made for explaining the Rufeh-Lieb anomaly by means of electron reflectivity effects.

It has been suggested by workers in the Soviet Union that the Rufeh-Lieb anomoly may be due to patch effects since the initial investigations used a diode with polycrystalline electrodes. However, later investigations (see Reference 3) using a guarded diode with oriented electrodes gave the same result.

C. DISCREPANCIES IN COLLECTOR WORK FUNCTION DETERMINATIONS

Collector work function in a thermionic converter is measured either by back emission or retarding potential methods. For cesiated metal electrodes, these two methods usually give consistent values. However, collectors formed with cesium-oxygen composites frequently give inconsistent results. An example (titanium oxide collector) is given in Figure 9. Early in the diode life, the discrepancy between the back emission and retarding potential determinations are pronounced. After the diode was aged, the two measurement methods gave consistent results.

Another example of discrepancies in back emission and retarding potential determinations is shown in Figure 10. These data are for a converter with a lanthanum hexaboride collector. Since the measurements given in Figures 9 and 10 were made with unguarded variable spaced diodes, these data are somewhat suspect.

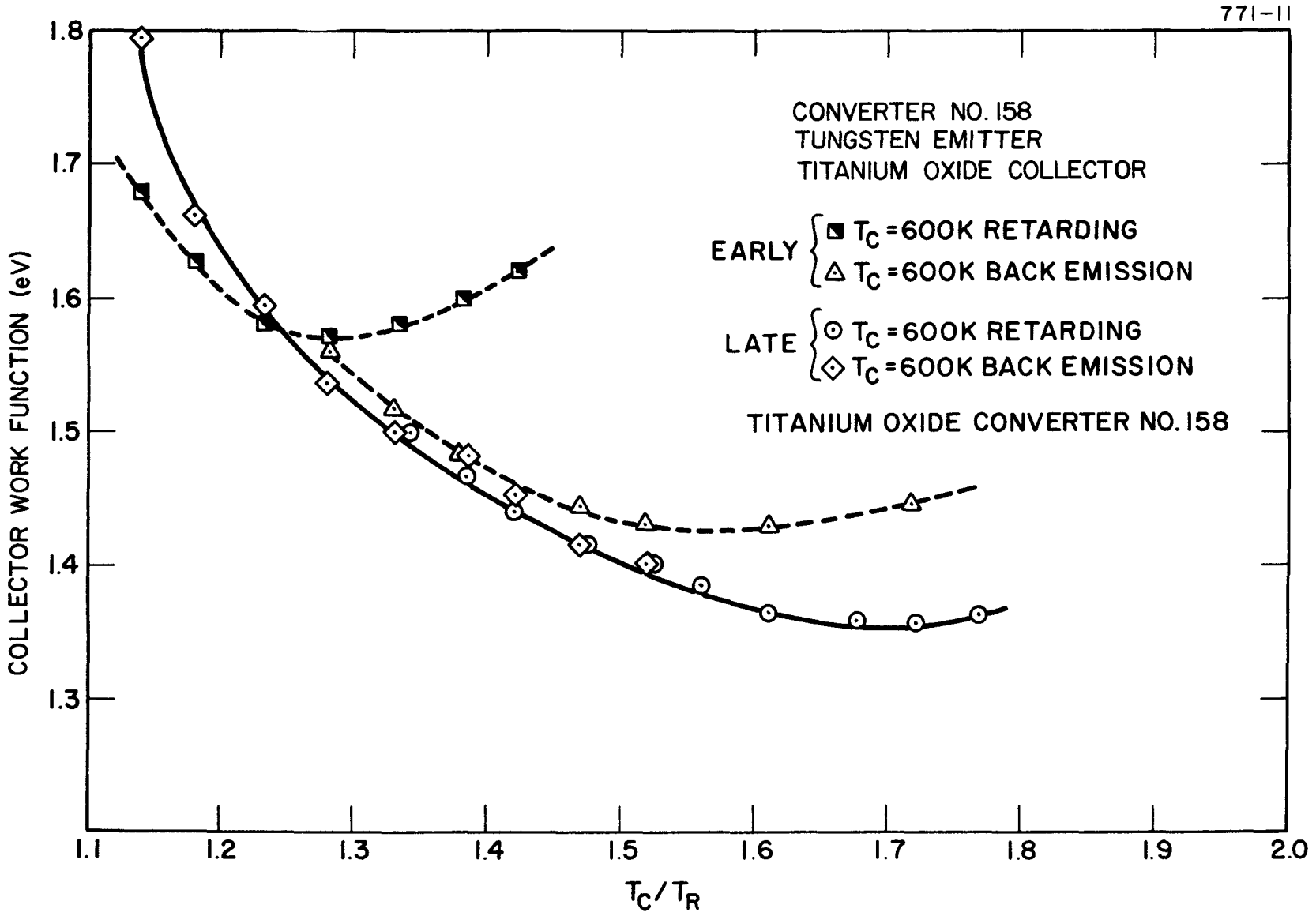

Figure 9. Retarding and Back Emission Collector Work Function Measurements

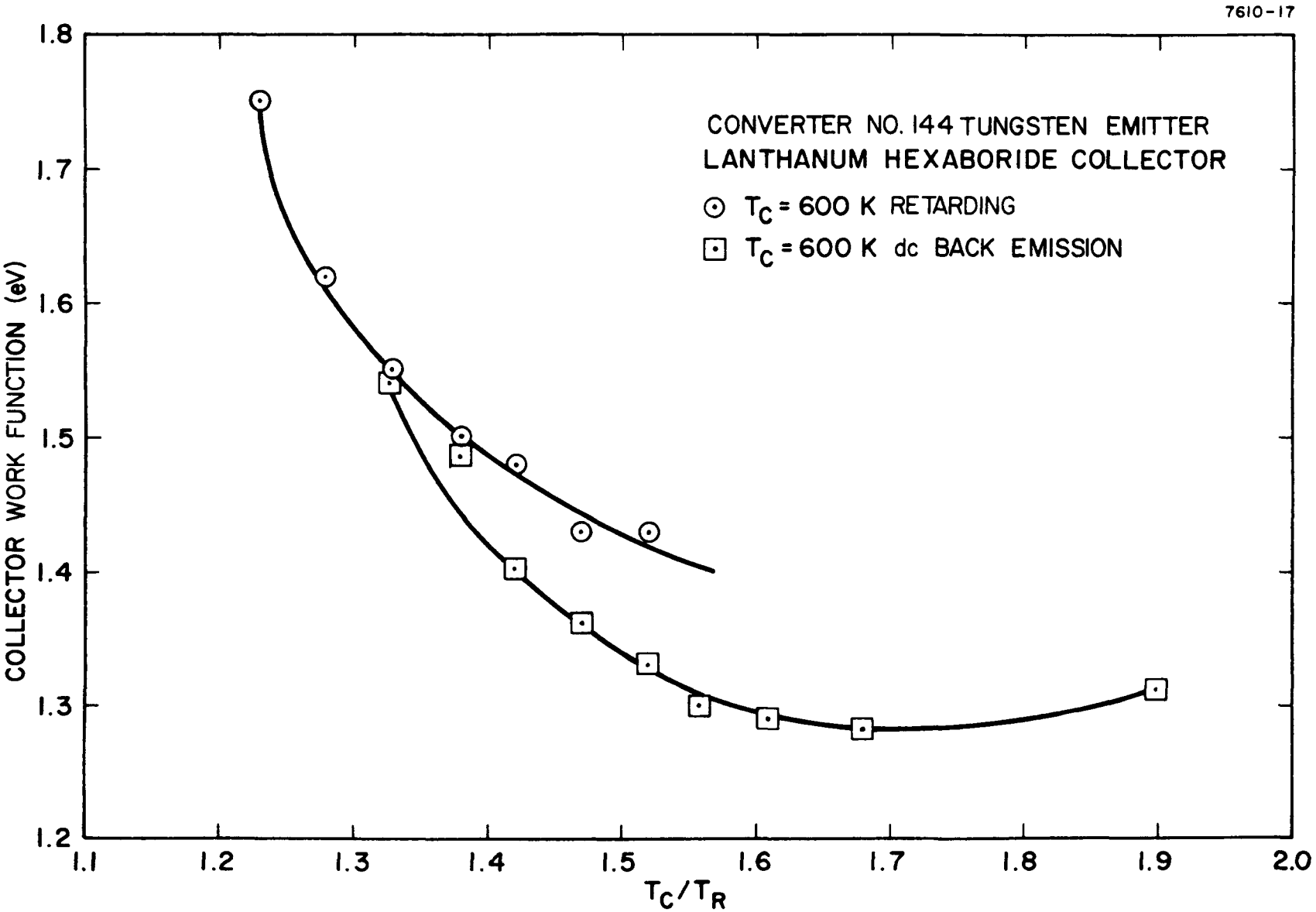

Figure 10. Lanthanum Hexaboride Collector Work Function versus T_C/T_R

In order to eliminate such reservations, measurements were taken with the guarded collector variable spaced converter shown in Figure 11. This converter had a platinum emitter and a nickel collector. The emitter temperatures and operating time were such that appreciable platinum would be expected to vaporize onto the collector during the test period. Initial and final collector work function data for this converter are shown in Figure 12. Again, the discrepancy in back emission and retarding potential work functions is evident. This discrepancy becomes less pronounced with time. Note that these measurements were performed on a guarded collector converter with metal electrodes at identical spacings, cesium pressures and electrode temperatures. The magnitude of the work function difference is well outside the limits for non-systematic error.

Additional collector work function data were taken at intermediate stages of testing. It is interesting to plot the difference between the retarding potential and back emission collector work functions versus the minimum value of the back emission determination for a given stage, parametric in the ratio of collector and cesium reservoir temperatures. Such a plot is shown in Figure 13. This figure indicates a systematic shift in collector work function characteristics during the test period of this diode. It is surprising that the data points on such an expanded scale shown such moderate scatter. The difference between the retarding potential and back-emission collector work function values becomes more pronounced with decreasing work function (as measured by back-emission).

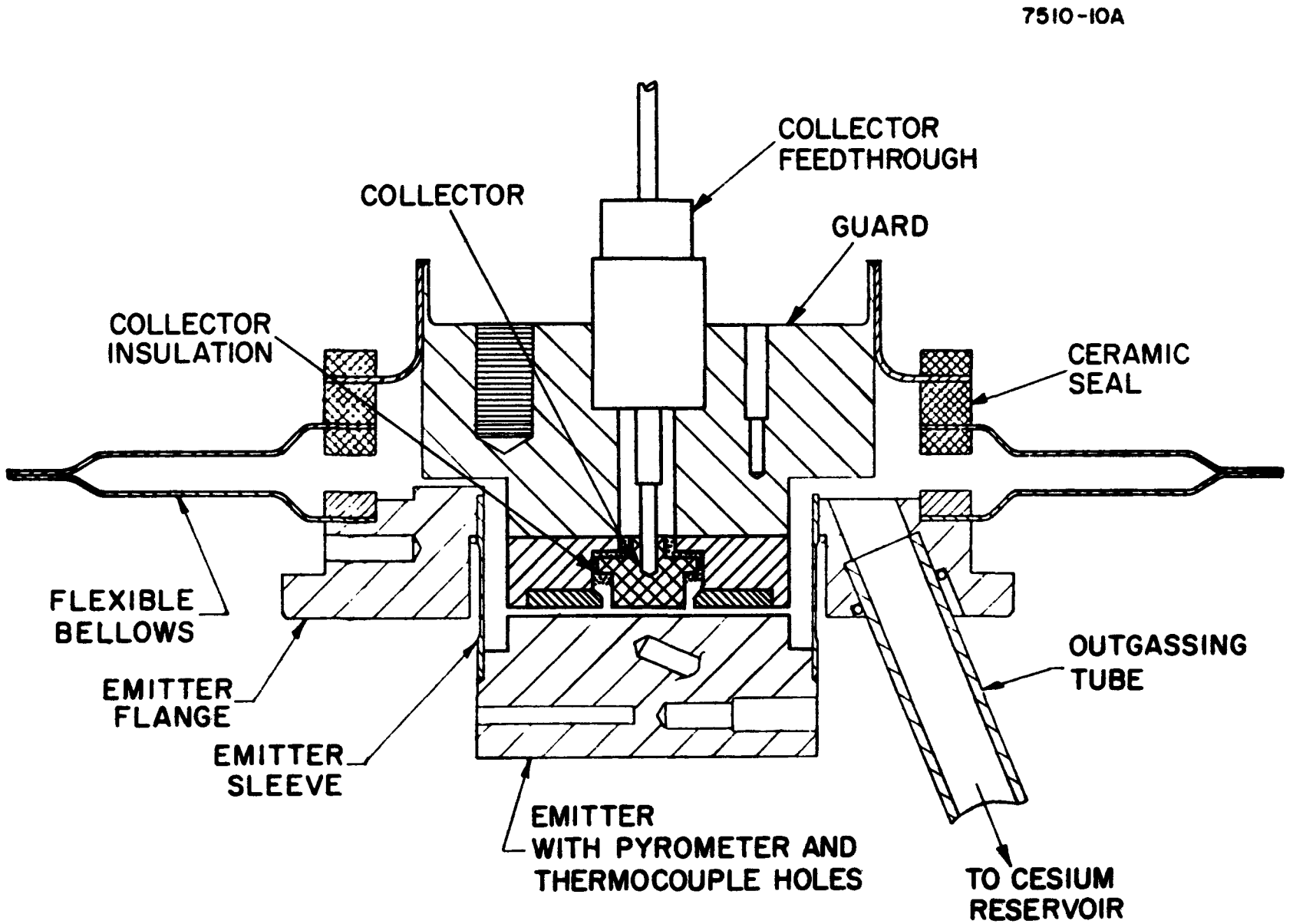

Figure 11. Guarded Converter with Platinum Emitter and Nickel Collector

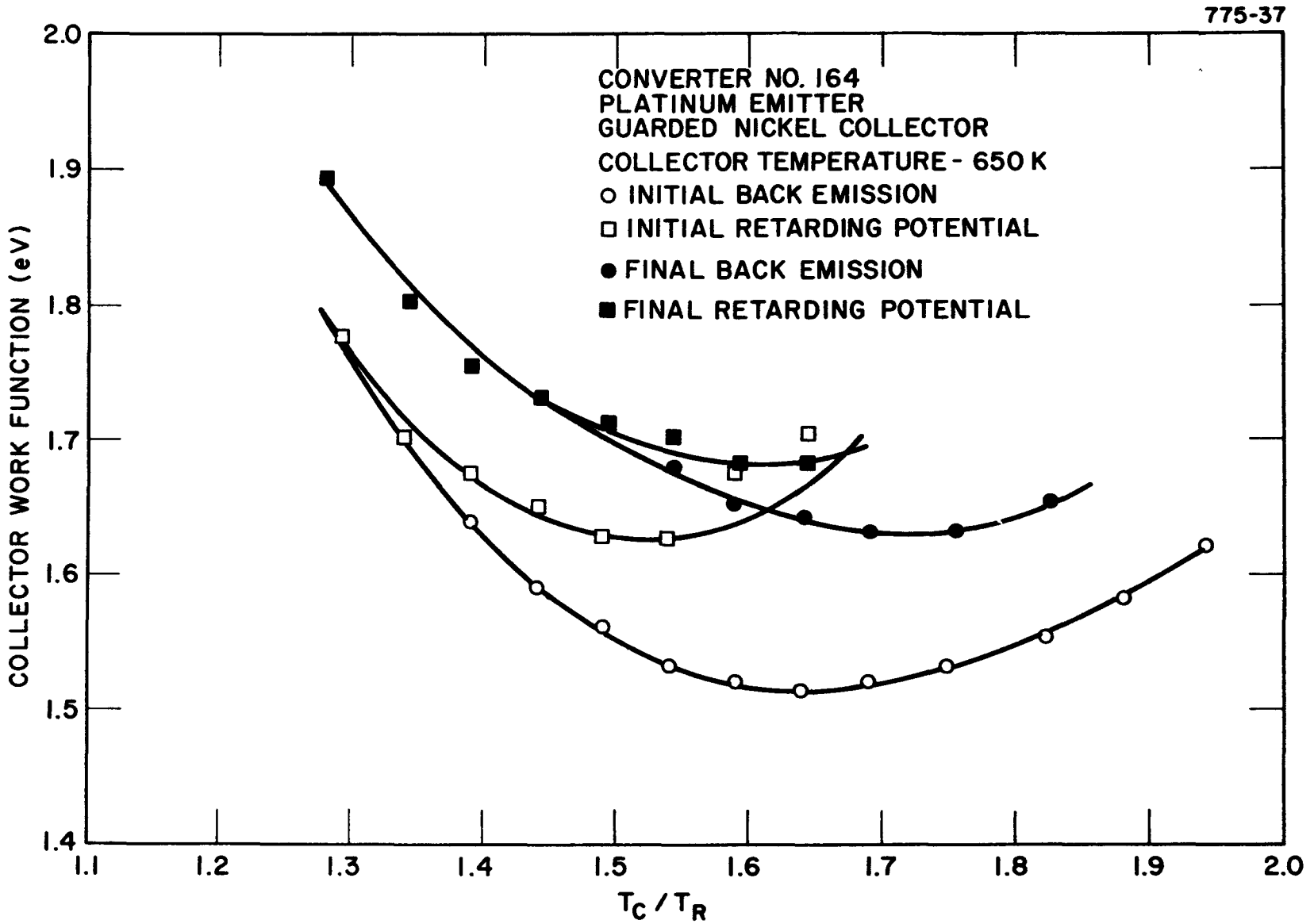

Figure 12. Comparison of Initial and Final Collector Work Function Determinations for Converter No. 164

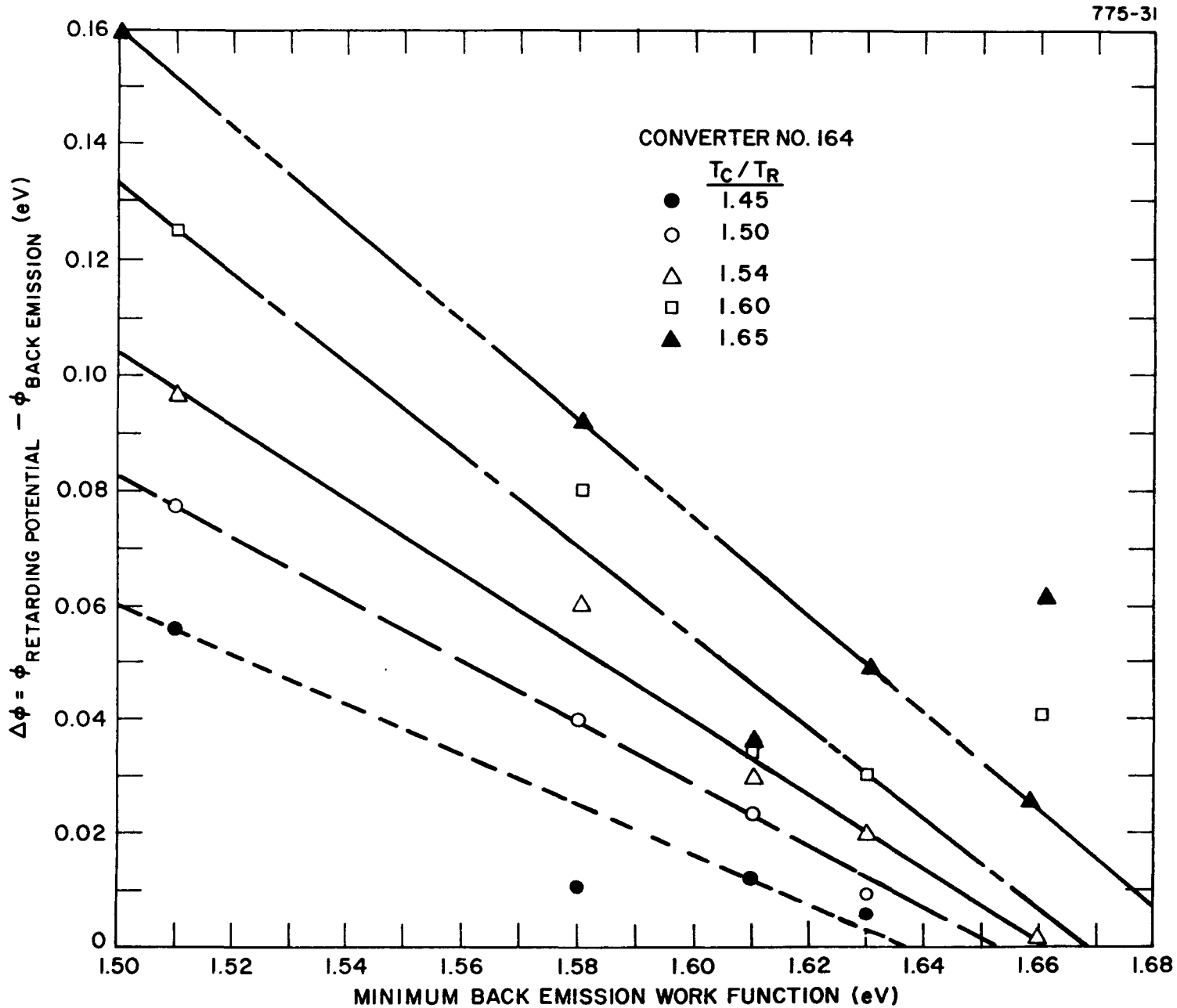

Figure 13. Difference Between Retarding Potential and Back Emission Collector Work Functions versus Minimum Back Emission Work Function for Converter No. 164

It was expected that the collector work function would change during the test period because the emitter temperature was deliberately raised to 1625 K (for periods of one hour with cesium reservoir cold) on three occasions to evaporate platinum onto the collector. Thus, the data in Figure 13 represent a nickel collector (probably oxidized) which becomes progressively more covered with platinum with each evaporation. Based on vapor pressure data in the literature, the final work function determinations correspond to a collector with multiple layers of platinum. However, these considerations do not represent an explanation of the discrepancy between the back-emission and retarding potential determinations of collector work function.

The shapes of the collector work function curves in Figures 9, 10 and 12 look suspiciously like those given in Figure 8 which illustrate the Rufeh-Lieb anomaly. This similarity may be more than accidental since the current flow in the retarding potential measurement is in the same direction as that in an operating converter.

One interpretation of the data in Figures 9, 10 and 12 is that the retarding potential determination shows the effect of electron reflectivity. However, this interpretation is clouded since a similar reflectivity would be expected for the back emission electrons. Alternative explanations invoke patches, rectifying junctions and negative ions.

D. LANTHANUM HEXABORIDE CONVERTER DATA

Lanthanum hexaboride is one of the most interesting electrode materials for emitters and/or collectors. This refractory compound is stable at temperatures up to 1700 K and has a low enough work function for practical current densities without cesium. Although lanthanum hexaboride has many promising characteristics, the role of impurities, stoichometry and crystallinity in this material are not well understood.

A summary of four recent diodes built with LaB_6 collectors is given in Table I. All four diodes are quite different in configuration, materials and processing.

The first Thermo Electron diode gave a better than average barrier index of 2.0 eV with the lowest measured work function of 1.35 eV. This encouraged the construction of a second diode which allowed oxygen to be diffused through the sintered collector - analogous to a showerhead (see Figure 14). The collector work function data for this converter is given in Figure 15. Alternate exposures of the LaB_6 to cesium and oxygen lowered its work function to 1.2 eV at 550 K and 1.25 eV at 600 K. Note the good agreement of the back emission and retarding potential measurements. These values represent the lowest work functions ever measured at Thermo Electron with any collector material in a converter configuration. However, the barrier index of this diode ranged around 2.2 eV. On the basis of a simple diode model, a much lower barrier index around 1.75 eV would have been expected. Indeed, investigators in the Soviet Union have reported such a low barrier index in a diode with a LaB_6 collector.

TABLE I

DIODES WITH LANTHANUM HEXABORIDE COLLECTORS

ORGANIZATION	MINIMUM COLLECTOR WORK FUNCTION (eV)	BARRIER INDEX (eV)	COLLECTOR MATERIAL	EMITTER MATERIAL
THERMO ELECTRON	1.35	2.0	SINTERED CERAC™ LaB_6 (SILVER TUBE O_2 INLET)	POLYCRYSTALLINE TUNGSTEN
THERMO ELECTRON	1.25	2.2	SINTERED CERAC LaB_6 (SHOWERHEAD O_2 INLET)	POLYCRYSTALLINE TUNGSTEN
SUKHUMI (USSR)	1.2	1.75	SINTERED LaB_6 POWDER ON TOP OF Ta POWDER	(110) TUNGSTEN
LEWIS RESEARCH CENTER (NASA)	—	1.9	HIGH PURITY ARC MELTED LaB_6	HIGH PURITY LaB_6 POWDER SINTERED IN CARBURIZED TANTALUM CUP

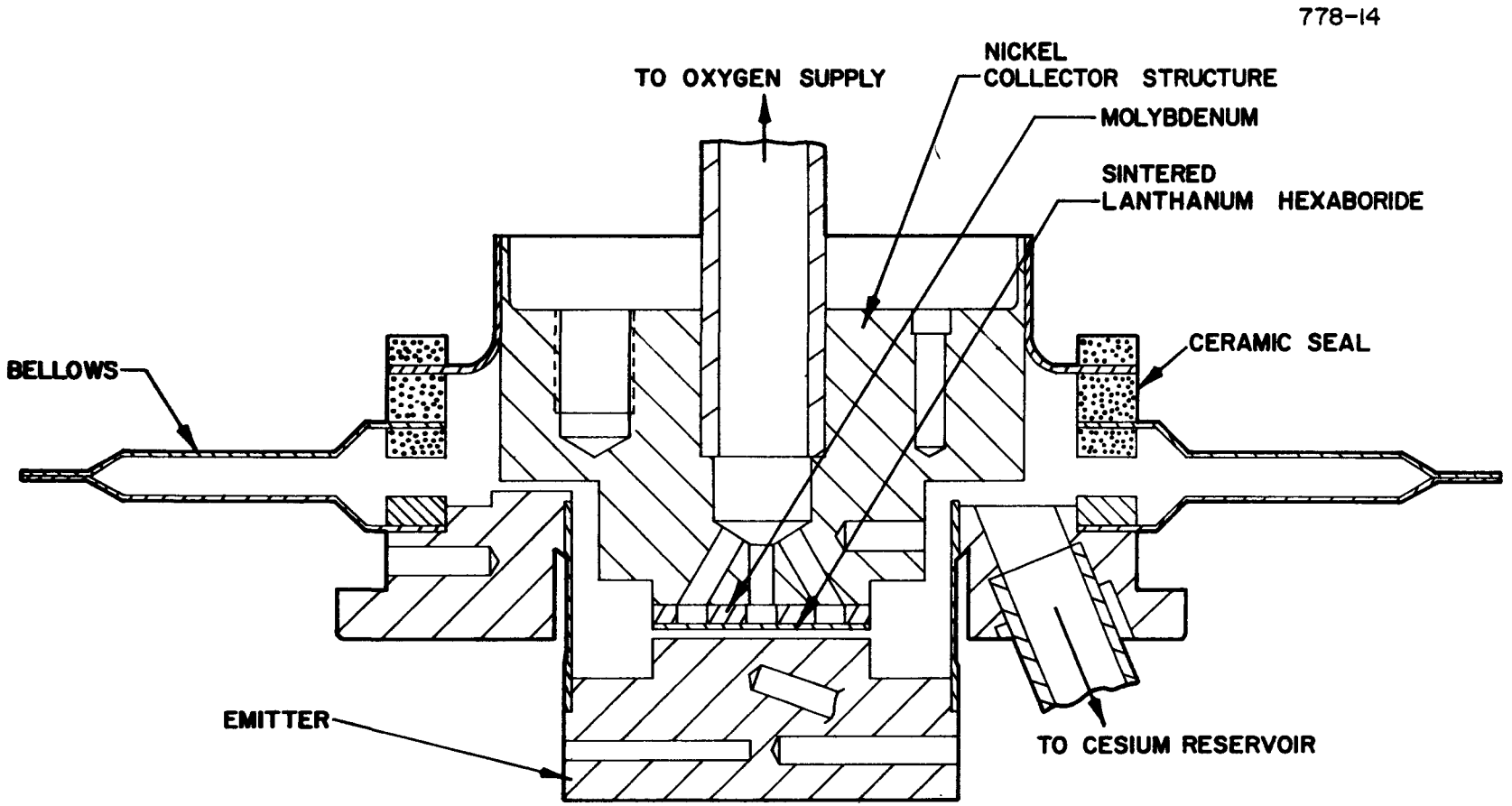

Figure 14. Showerhead Diode with Lanthanum Hexaboride Collector

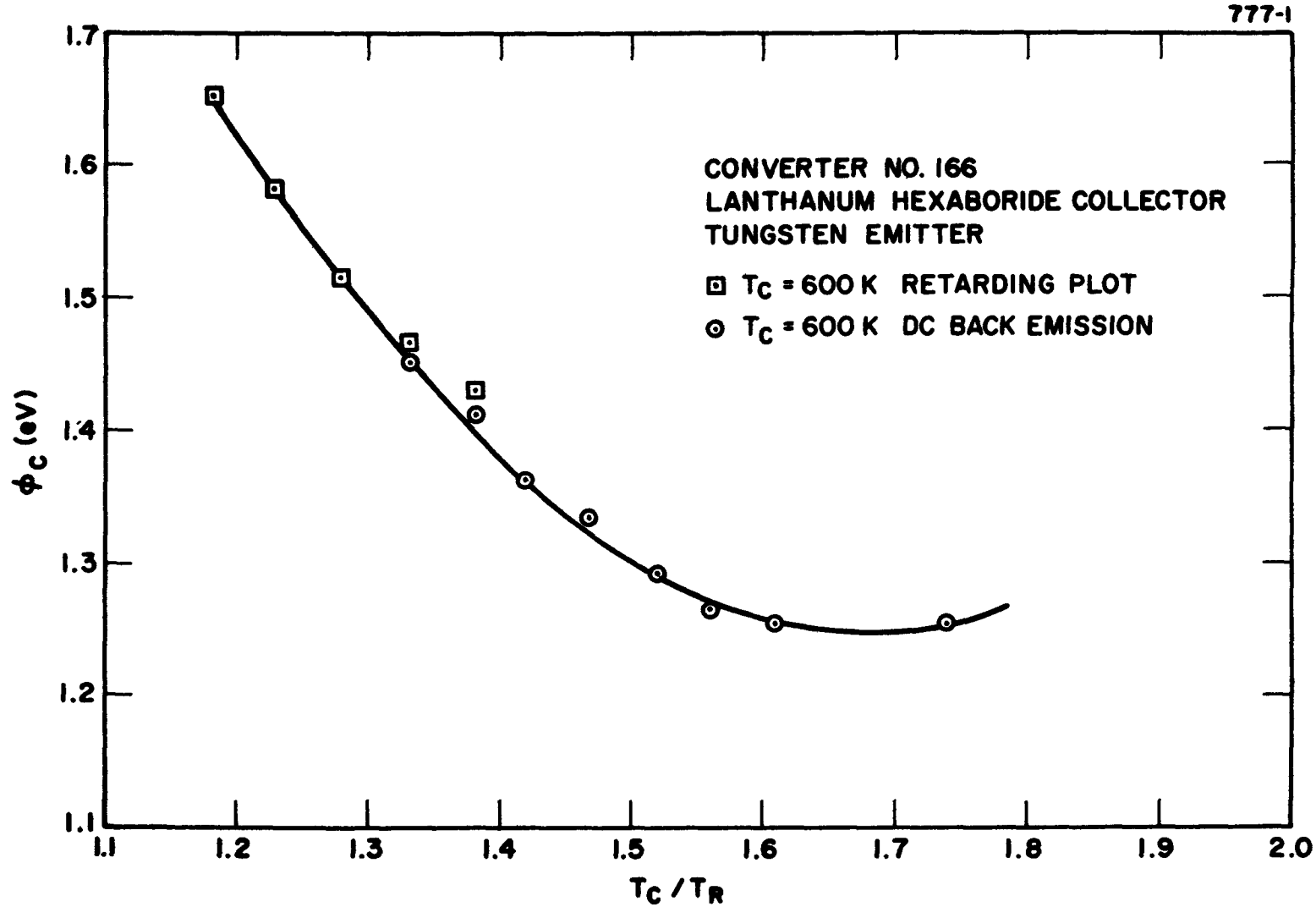

Figure 15. Lanthanum Hexaboride Collector Work Function in Showerhead Diode

Recent results from the Lewis Research Center fall between those from Thermo Electron and the Soviet Union.

Assuming that the unpublished data from Sukhumi are valid, there is a discrepancy of almost half an electron volt in barrier index between the Soviet Union and the Thermo Electron diodes - although they agreed well in regard to minimum collector work function. In addition, the relationship between the collector work functions and barrier indices of the two Thermo Electron diodes are opposite from that expected. If the data in Table I are taken at face value, it is clear that the performances of these diodes with LaB_6 collectors are highly inconsisent.

It is possible that these discrepancies are related to collector electron reflectivity effects. Thus the Thermo Electron showerhead diode may represent a LaB_6 electrode with a low work function, but a high electron reflectivity while the Sukhumi diode may represent a LaB_6 collector with both a low work function and a low electron reflectivity.

E. HEAT FLUX MEASUREMENTS

Although back emission and retarding-mode measurements are two methods for determining the collector work function in converters, neither can be applied under ignited-mode conditions. An independent technique that can be used in this regime is based on measuring the heat flow into the collector as a function of converter current.[4]

Assuming an elementary model of the thermionic diode, the thermal flux, q, into the collector is composed of energy carried by the electrons constituting the current, the radiation from the emitter and the convection from the emitter through the plasma to the collector. Thus,

$$\dot{q} = j(\phi_c + 2kT_e) + r + c \qquad (1)$$

where j is the current density into the collector, ϕ_c is the collector work function, T_e is the electron temperature of the plasma at the collector, and r and c define the radiative and convective components, respectively. Differentiating Equation 1 with respect to the current, j, at constant electrode temperatures, and assuming constant T_e, defines an "effective heat transport factor"

$$\zeta = \phi_c + 2kT_e \qquad (2)$$

An accurate determination of this parameter requires precise measurement of the change in $\dot{q}$ as j is varied. In order to minimize the interpretation of heat transfer effects caused by the complex geometry of the converters, a heat flux diode was constructed with a thermally "nulling" auxiliary heater positioned 0.75 mm from the collector surface. The design of the heat flux diode is shown in

Figure 16. The emitter is polycrystalline tungsten and the collector is nickel. As the current through the diode was varied (and, correspondingly, the temperature of the collector changed), the power of the auxiliary heater was adjusted until the collector was returned to its initial temperature. The increase (or decrease) in the auxiliary heater power represents the change in $\dot{q}$.

Precise and rapid measurements of $\dot{q}$ require coordinated adjustment of the auxiliary power in a manner to maintain almost constant emitter and collector temperatures as the current is substantially varied. It is possible to maintain the emitter at 1600 $\pm$ 1 K and the collector at 850 $\pm$ 0.2 K.

A block diagram of the experimental arrangement is shown in Figure 17. The cooling water for the collector was maintained at a constant temperature of 305 K in order to avoid fluctuations in the baseline temperature of the collector. The power to the auxiliary heater, the most critical measurement in the experiment, was monitored by the computer. Auxiliary heater voltages were measured by taps located as close as possible to the heater element. The auxiliary current was measured by a calibration shunt. These voltages and currents were sampled at five-second intervals by the computer, which calculated the instantaneous heater power, its running average, and its total average. The error in this power measurement was less than 0.02 W.

After the current was varied, a thermal equilibration time of five minutes was allowed before data were taken. The auxiliary heater power was then averaged over a 10-minute period in order to

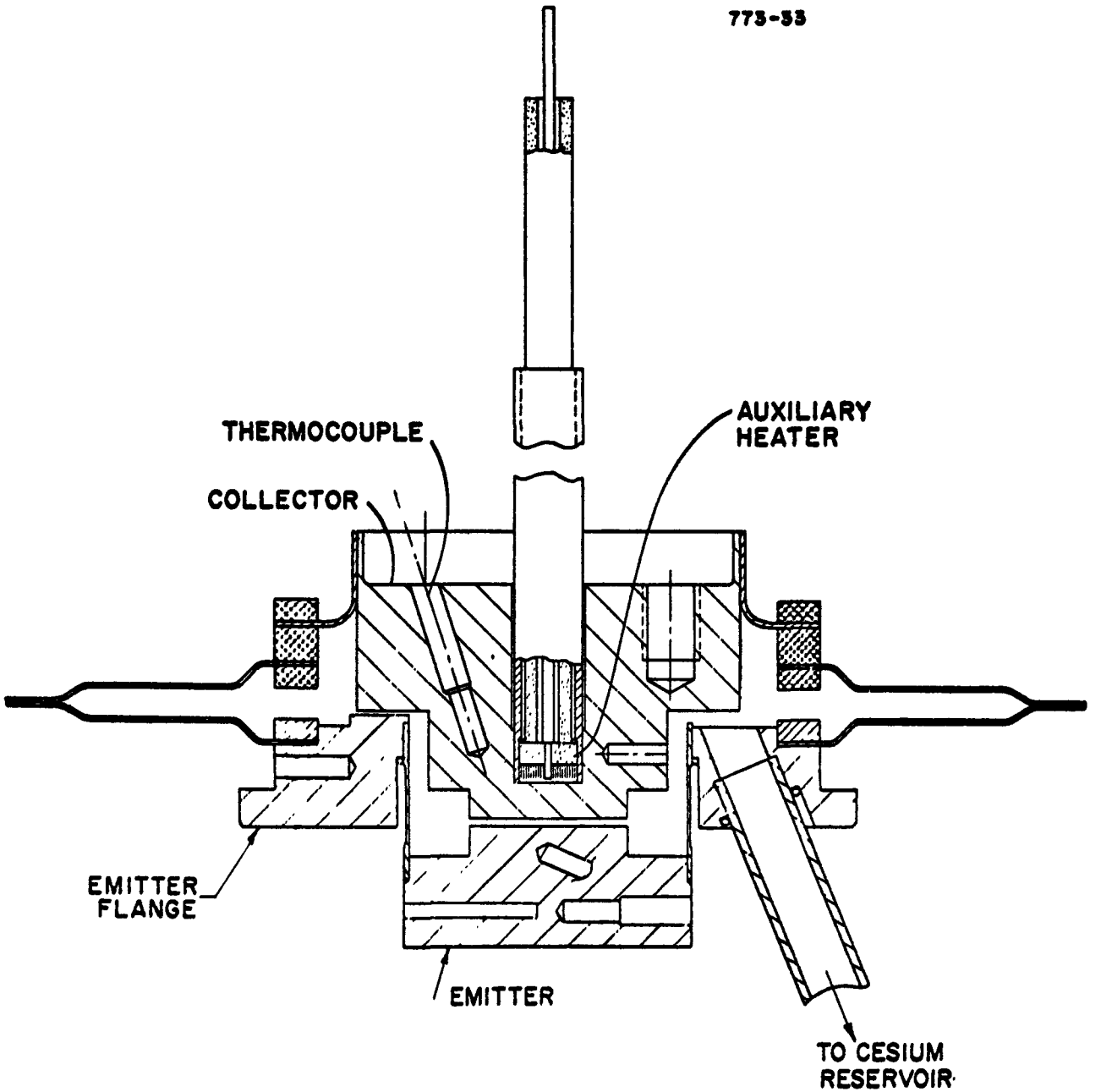

Figure 16. Heat Flux Diode

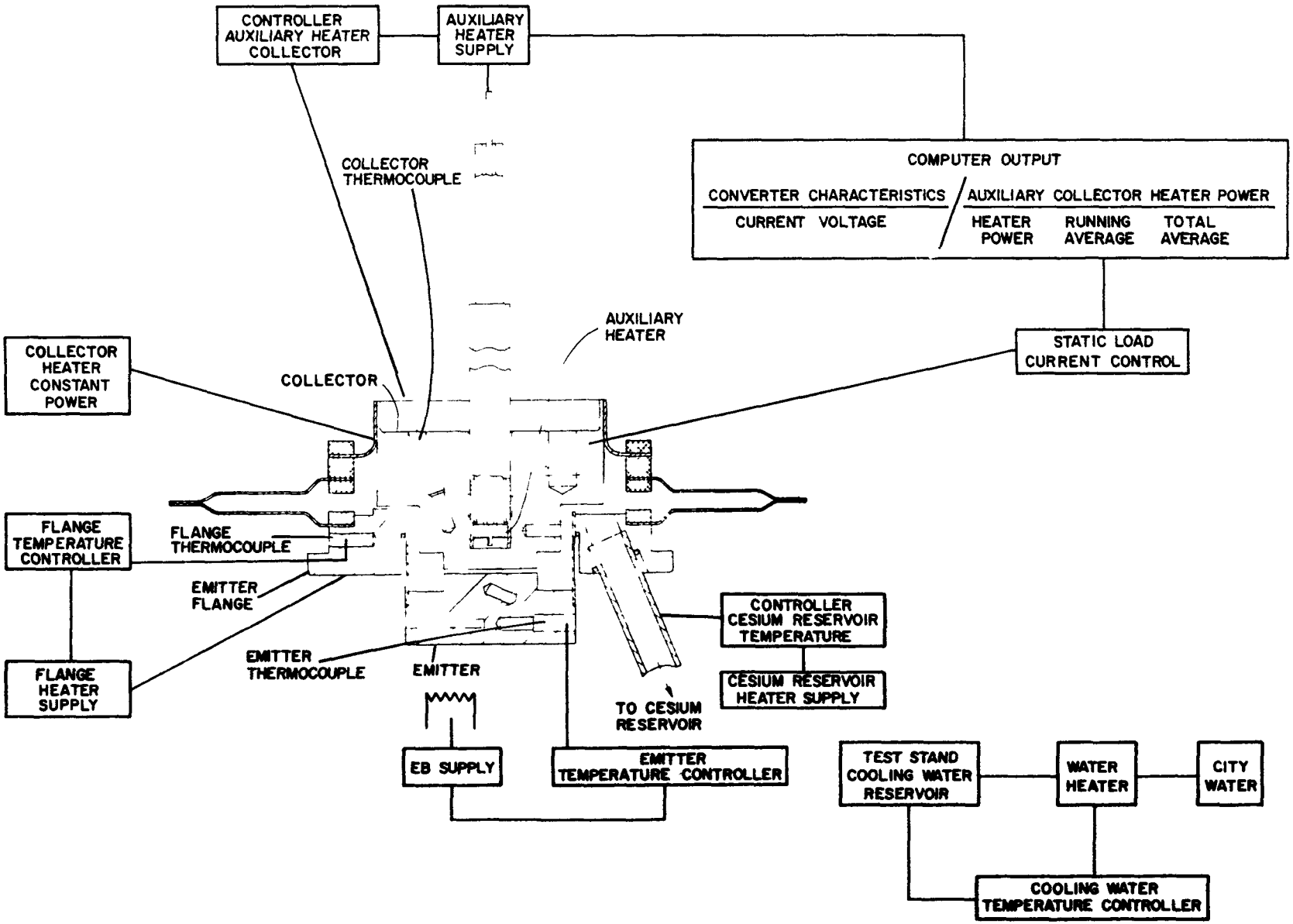

Figure 17. Block Diagram of Heat Flux Experiment

minimize fluctuation effects. A representative curve of auxiliary power versus converter current is shown in Figure 18. The reproducibility of the data is illustrated by the good comparison of points recorded on different dates.

Collector work function versus T_C/T_R is given in Figure 19. Typical current-voltage curves for variable cesium reservoir temperatures are shown in Figure 20. Current-voltage characteristics, parametric in collector temperature, are given in Figure 21. The operating points at which heat flux determinations were made are indicated in this figure.

Heat flux measurements were made at interelectrode spacings of 0.05, 0.5, and 2 mm. The converter current was varied between one and 5 A. Figure 22 contains curves of the heat flux measured at these spacings and currents. A least-squares fit was used to determine the straight line slope representing the effective collector work function . These results imply a collector work function at least 0.3 eV larger than expected from back emission and retarding measurements (assuming an upper limit of 0.25 eV on the electron temperature). The range of parametric variation in $\dot{q}$ and j will be extended in the hope of identifying phenomena that may explain this discrepancy.

Electron reflectivity may account for the apparent collector work function discrepancy. If one assumes a slightly more sophisticated diode model than considered previously, the measured current, j, is related to the incident current, J, and electron reflectivity of the collector, R, by

$$j = (1 - R)J \qquad (3)$$

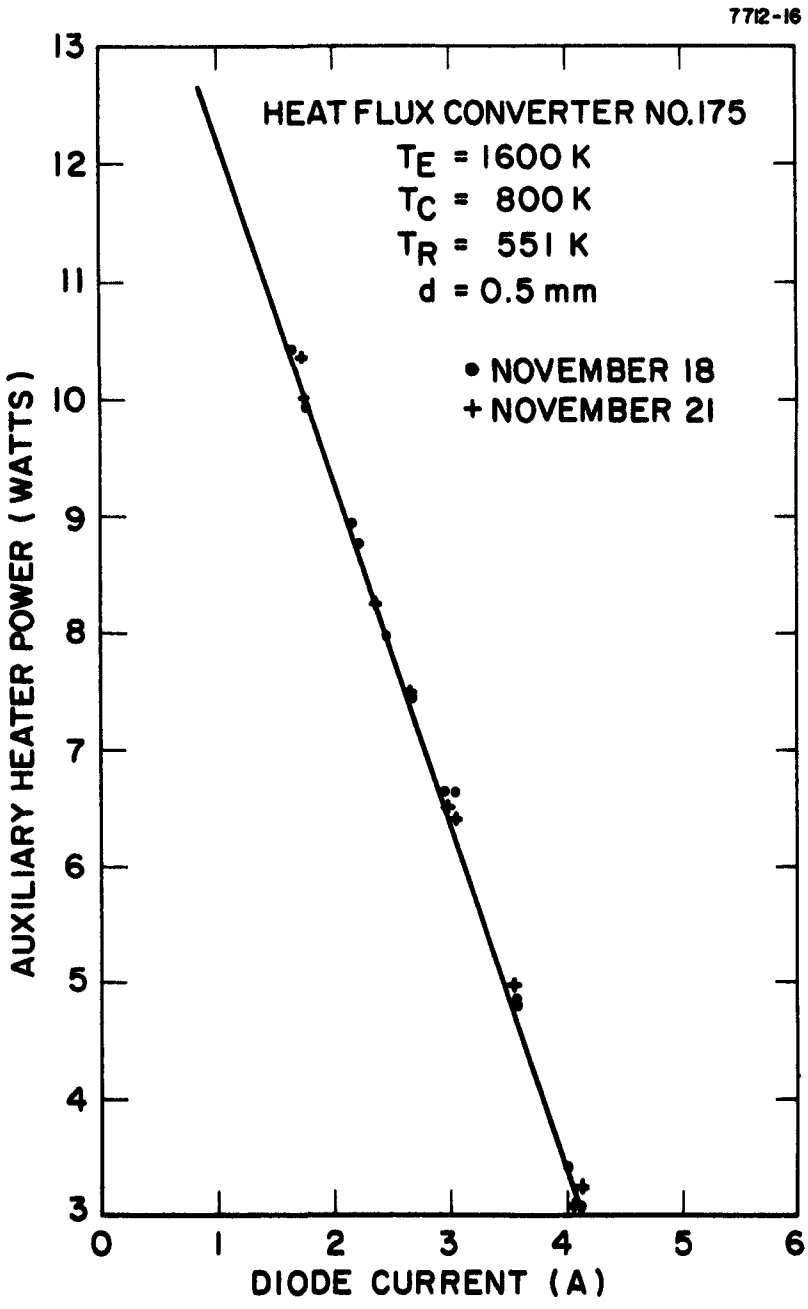

Figure 18. Heat Flux Data

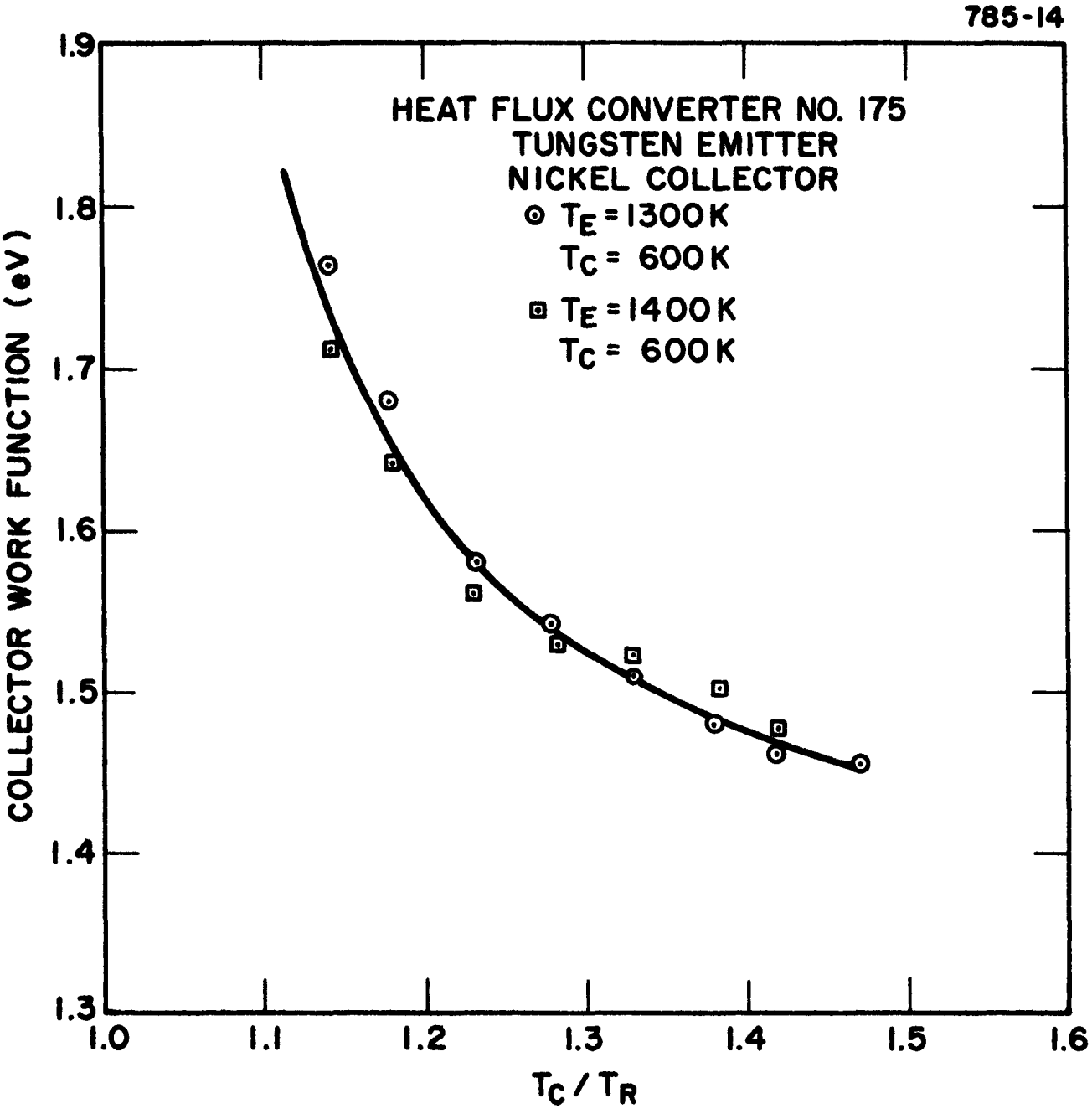

Figure 19. Collector Work Function versus the Ratio of Collector Temperature to Reservoir Temperature.

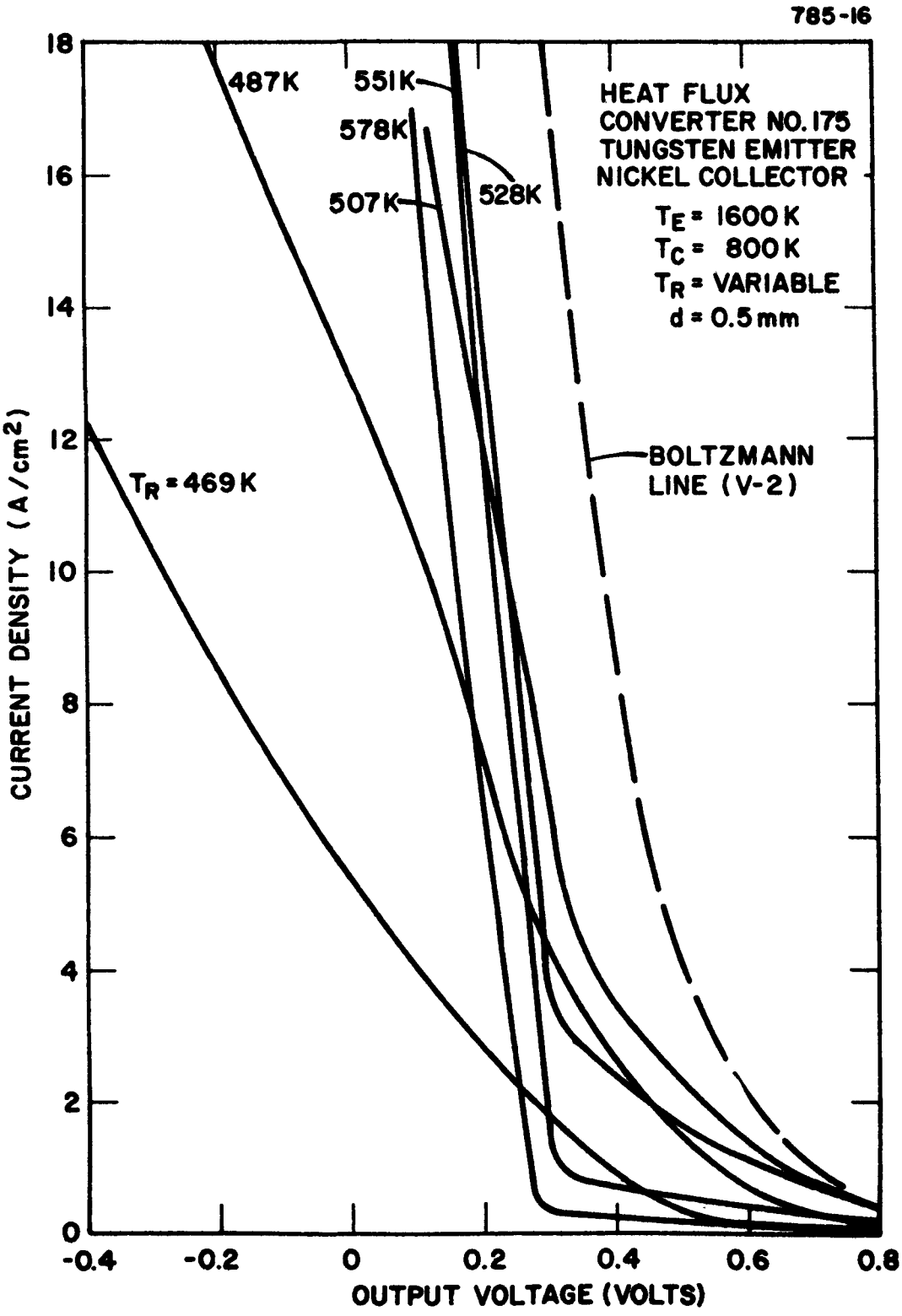

Figure 20. Typical Cesium Family for Heat Flux Converter No. 175.

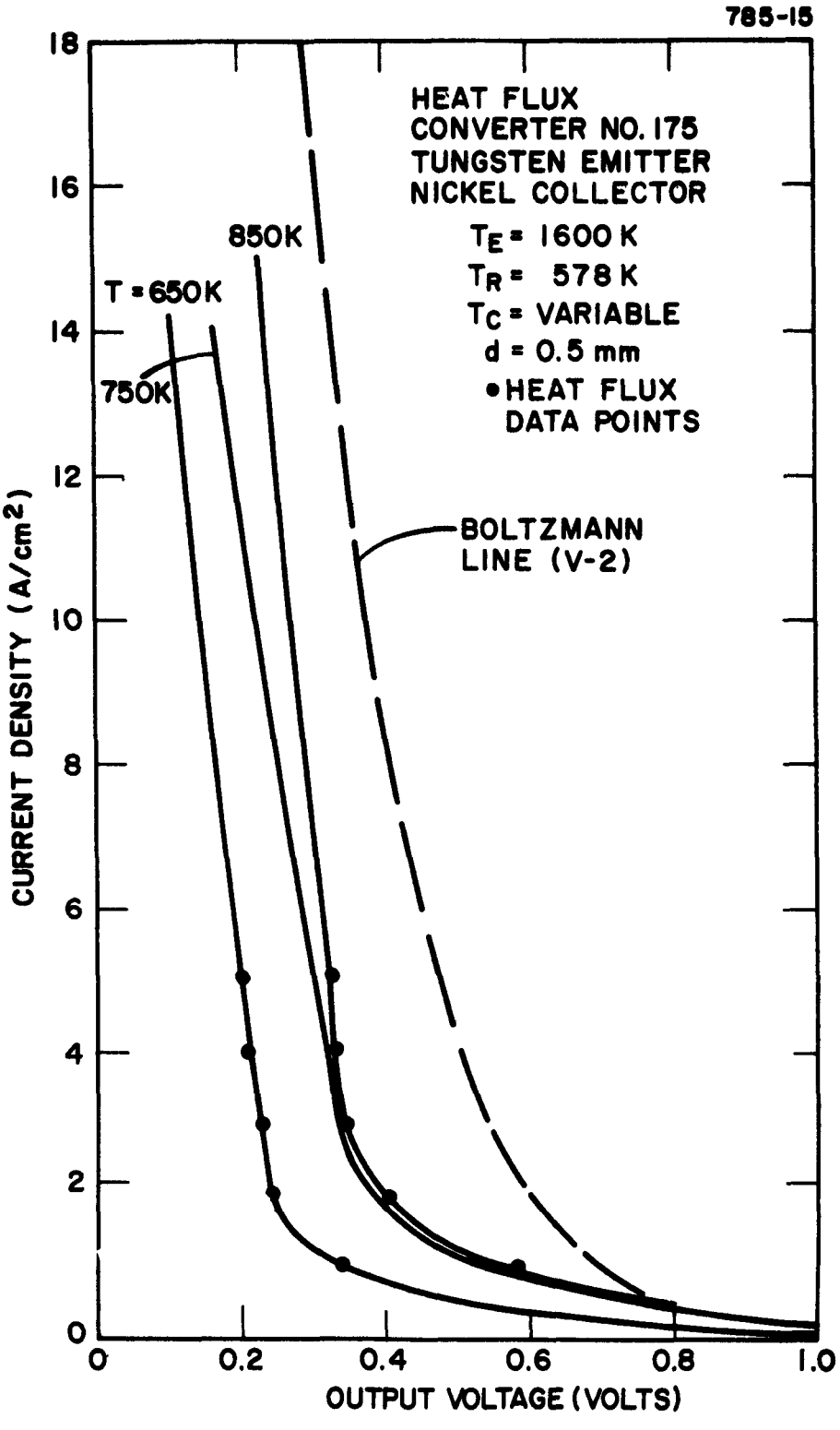

Figure 21. Collector Family for Heat Flux Converter No. 175.

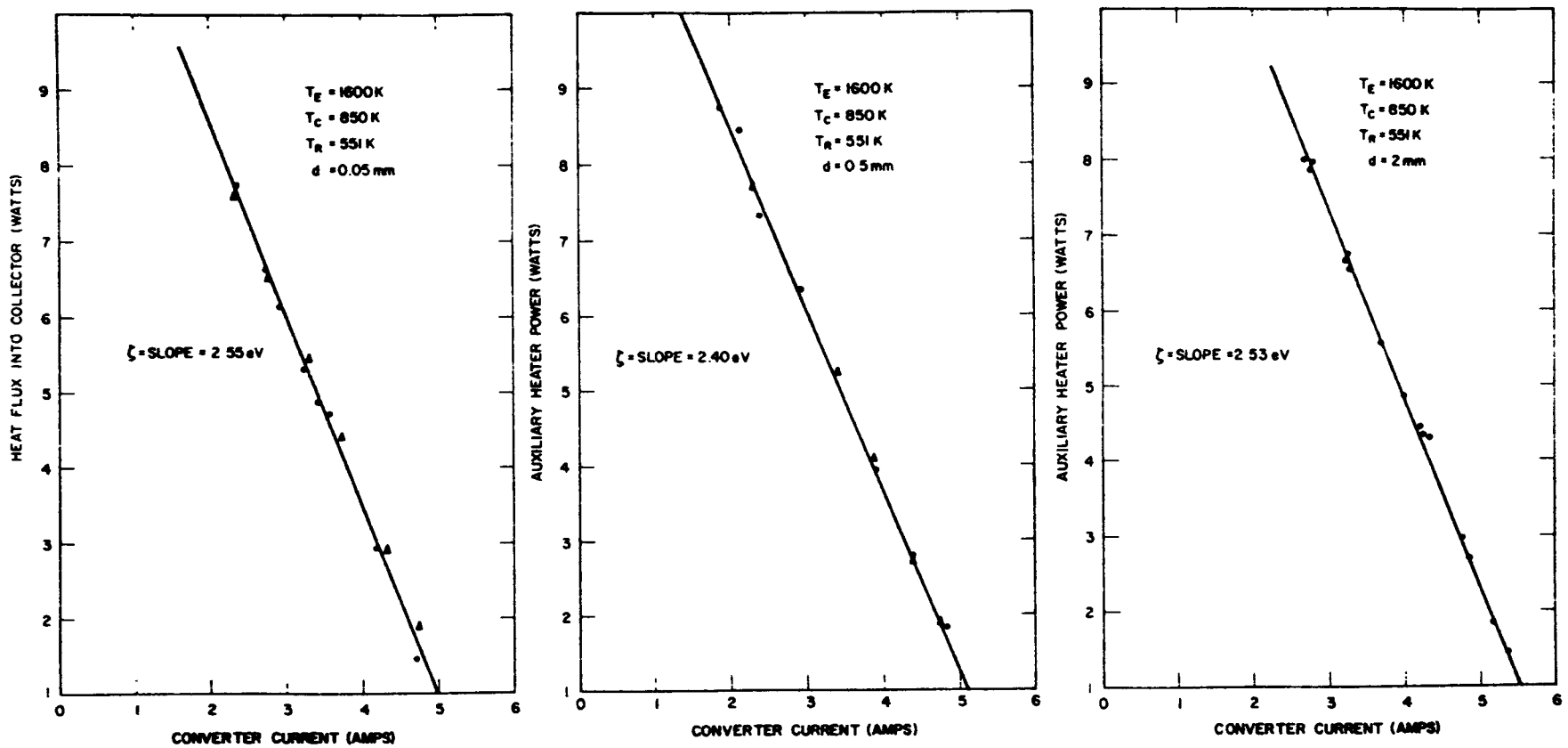

Figure 22. Effective Heat Transport Factors into Collector for Spacings of 0.05, 0.5, and 2.0 mm (Converter No. 175).

so that the heat balance on the collector is given by

$$\dot{q} = (1 - R)J(\phi_c + 2kT_e) + RJ\, f(T_e, T_C) + r + c \qquad (4)$$

where $f(T_e, T_C)$ represents the heat transport from the plasma into the collector per reflected electron. If the plasma electrons reflected by the collector are thermally equilibrated with this electrode, then

$$f(T_e, T_C) = 2kT_e - 2kT_C \qquad (5)$$

Possible mechanisms for thermal equilibration are phonon scattering and interaction with electron traps on and/or in the adsorbed cesium-oxygen layer. The expression in Equation 5 represents the maximum energy transport from the plasma into the collector by reflected electrons. Equation 4 can be rewritten as

$$\dot{q} = j(\phi_c + dkT_e) + \left(\frac{R}{1 - R}\right) j\left[2k(T_e - T_C)\right] + r + c \qquad (6)$$

Using the previous definition of the effective heat transport factor,

$$\zeta = \phi_c + dkT_e + \left(\frac{R}{1 - R}\right) 2k(T_e - T_C) \qquad (7)$$

For the data in Figure 22, T_C = 850 K, T_C/T_R = 1.54, and (from Figure 19) ϕ_c = 1.45 eV. If one assumes that R = 0.6 and T_e = 3000K, ζ = 2.52 eV, which is in good agreement with the experimental results given in Figure 22.

An electron reflectivity of 0.6 would not be expected with a cesiated nickel collector; however, if the collector is oxidized, such a value would not be surprising. Indeed, the data in Figures 19 through 21 are indicative of an oxygenated converter. An example of FERP reflectivity measurements taken previously at Thermo Electron is given in Figure 5. These determinations on a tungsten

substrate exposed to alternate doses of cesium and oxygen exhibit electron reflectivities (at a few tenths of an electron volt) around 0.5.

Another possible explanation of the high values of effective heat transport factors measured is that a portion of the energy associated with the plasma arc drop arrives at the collector and is converted into heat. The arc drop is the average useful energy lost per electron due to the combined effects of atomic excitation and ionization (inelastic scattering) and plasma resistivity (elastic scattering). Recombination and deexcitation eventually release the inelastic energy and radiate or convert this component to the electrodes. Similarly, energy is transferred by the elastic collisions from electrons to atoms and ions, and this portion will be converted and conducted to the electrodes as well.

F. DISCUSSION

The review of FERP measurements demonstrate that low work function electrodes formed by alternate exposures to cesium and oxygen sometimes provide significant electron reflectivities at thermal energies found in thermionic converters. Anomalies in converter output voltage versus collector work function, agreement of back emission and retarding potential collector work function determinations, lanthanum hexaboride diode performance and measurements of collector heat deposition per electron have been reviewed. In each case, the experimental data can be interpreted in terms of electron reflectivity effects. However, in no case is this interpretation unambiguous. Effects due to patch electrodes or negative ions could provide alternative interpretations for those anomalies.

In view of the wide variety in the electron reflectivity spectra for tungsten, molybdenum and gallium phosphide, it is difficult to draw general conclusions. However, the following statements can be made:

- Typically, low work function surfaces contain cesium and oxygen.
- Some low work function surfaces electron reflectivity.
- There is no apparent systematic relationship between work function and electron reflectivity (e.g., small changes in work function may involve large changes in electron reflectivity).

Electron reflectivity can have beneficial effects. For example, the shape of the 1.30 eV curve in Figure 5 corresponds to a surface with a low reflectivity at thermal energies and a high reflectivity to

electrons above one eV. Such an electrode would collect thermal electrons efficiently (constituting most of the converter current) while reflecting many of the incident hot electrons back into the interelectrode space where they could promote cesium ionization and reduce the arc drop in the converter. A converter with this kind of collector should have outstanding performance.

The balance of this report describes an analytical effort to characterize the dimensions and the potential configurations associated with the measured electron reflectivities. The analytical results are consistent with LEED studies of cesiated-oxygenated surfaces.[5]

BLANK

III. ANALYTICAL MODEL

The theoretical study described in this report was motivated by the realization, established in part by the experimental results discussed previously, that reflection of thermal electrons does occur and that it can be substantial. It is desirable to know the correspondence between the reflection coefficient and the variation of potential energy in the vicinity of the collector-plasma interface. The intent is to find a correlation between theoretical and esperimental reflectivity results. Once such correlations are drawn, attempts can be made to develop a fabrication procedure which would establish a surface composite having the desired characteristics.

It is largely accepted that cesium and cesium-oxygen surface layers produce a low work function by establishing a dipole layer with the positive side outer-most. This potential configuration is described in the idealized models shown in Figure 23. The step potential represents a clean, defect-free surface. The triangular surface barrier represents the effect of two parrallel and oppositely charged sheets. Such a model is descriptive of an adsorved monolayer of cesium ions and the resultant negative image in the metal substrate. The plus-minus configuration is also descriptive of a duo-layer of oxygen and cesium ions. The rectangular barrier, is an approximation for the mutilayered structures which have been observed experimentally - a positive surface separated from a negative metsl interface by a well-screened dielectric layer. Although one might justifiably argue that the top of the barrier should slope upward (instead of being flat), it should be kept in mind that the purpose of this purpose of this study is to establish a conceptual basis for electron reflection phenomena, rather than a detailed analysis. In addition, as will be discussed next, there are arguments

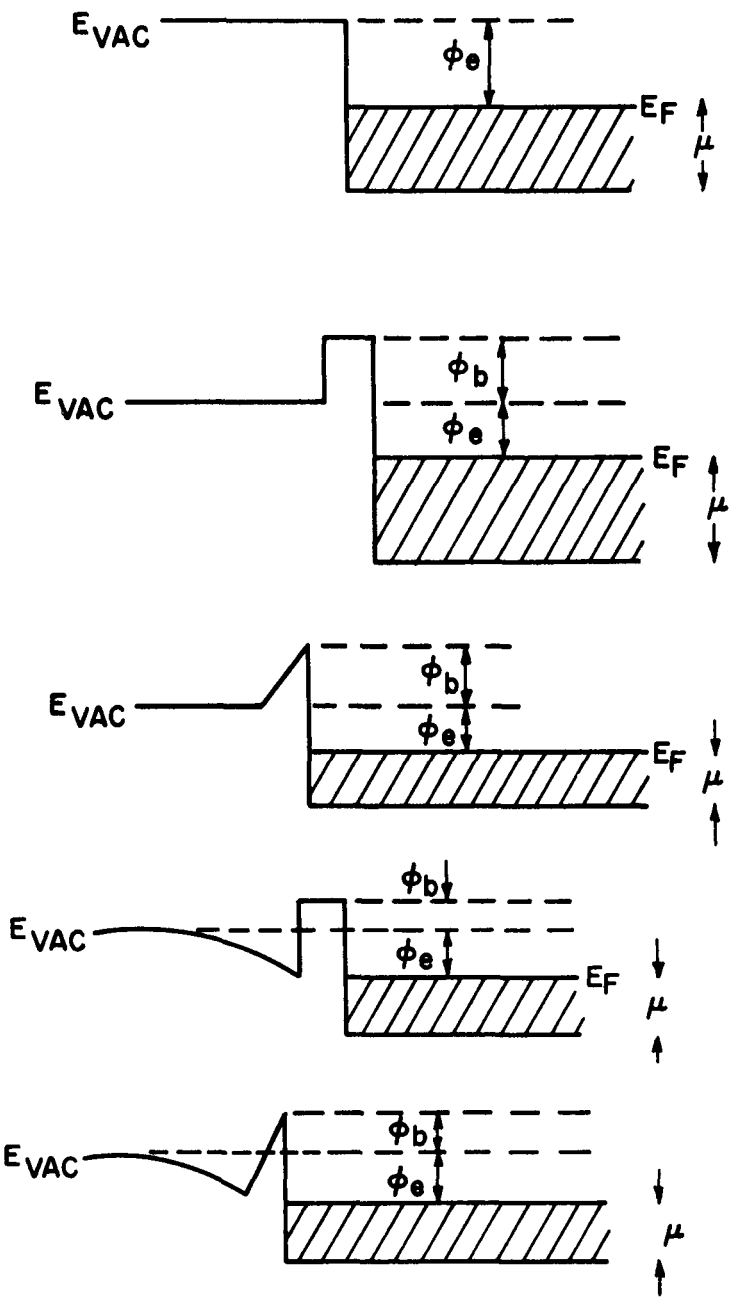

Figure 23. Potential Configurations for Analytical Models

for the top of the barrier being flat or sloping downward toward the substrate.

The effect of incorporating the finiteness of electron charge is depicted in Figures 23d and 23e. An electron approaching a conductor experiences an attractive image force resulting from the redistribution of free charge in the electrode in order to cancel the field of the electron inside the material. Superposition of image and surface barrier potentials should result in a net reduction of the surface barrier maximum, a reduction or reversal in the slope of the triangular barrier and a downward sloping of the rectangular barrier toward the underlying metal. However, the point of termination of the image potential is not clearly defined. At distances of the order the electron mean free path in the metal ($\sim$100 Å), one can expect the classical image field concept to break down. At these dimensions, point exchange and correlation effects become dominant. Since this distance is of the order greater than the barrier thicknesses of interest, it was decided to restrict the models discussed in this report to the simplicity shown in Figure 23.

The mechanism of electron collection is indicated in Figure 24. The axial symmetry about the normal to the surface barriers discussed in this report allows the separation of coordinates of the general three dimensional Schroedinger equation. Since a steady-state situation is being considered, there is no detailed analysis of the behavior of moving wave packets as a function of time. Therefore, the time independent Schroedinger equation is used. The general mathematical statement of this equation in one dimension can be stated as follows:

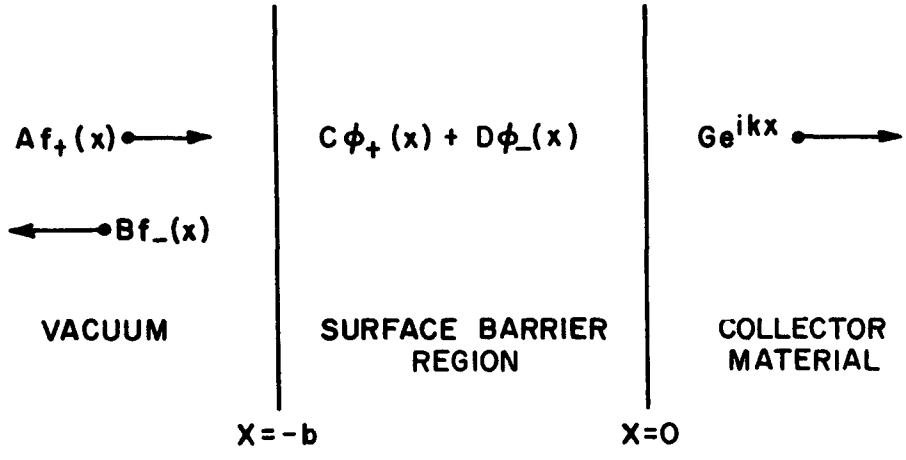

Figure 24. Model of a Generalized Encounter of Incident Electrons with Collector Covered by a Surface Barrier

$$\frac{h^2}{2m}\frac{d^2\phi(x)}{dx^2} + V(x)\,\phi(x) = E\phi(x) \tag{8}$$

where all pertinent symbols are defined in the Glossary of Symbols. The electron reflection coefficient is determined by the ratio of the probability density currents from and toward the surface. The values of these currents are easily determined in the free electron case, where solutions can be readily stated in the form of traveling waves (e^{ikx}, e^{-ikx}). Since we are interested only in the physical situation of an electron incident from the vacuum and its reflection or transmission from the surface barrier, we start with positive ($f_+(x)$) and negative-going ($f_-(x)$) traveling waves in the vacuum and a positive-going wave in the substrate.

The vacuum wave functions ($f_+(x)$) and ($f_-(x)$) asymptotically approach positive and negative traveling waves as infinite. The combination $C\phi_+(x) + D\phi_-(x)$ is the most general expression for describing the electron wave in the surface barrier region. On the basis of the model depicted in Figure 23, the reflection coefficient can be stated as

$$R = \frac{|B|^2}{|A|^2} = \frac{\begin{vmatrix} \phi_+(-b) & 0 & -f_+(-b) & -f_-(-b) \\ \phi'_+(-b) & 0 & -f'_+(-b) & -f'_-(-b) \\ 0 & 1 & f_+(0) & f_-(0) \\ 0 & ik & f'_+(0) & f'_-(0) \end{vmatrix}}{\begin{vmatrix} 0 & \phi_-(-b) & -f_+(-b) & -f_-(-b) \\ 0 & \phi'_-(-b) & -f'_+(-b) & -f'_-(-b) \\ 1 & 0 & f_+(0) & f_-(0) \\ ik & 0 & f'_+(0) & f'_-(0) \end{vmatrix}} \tag{9}$$

BLANK

IV. ANALYTICAL RESULTS

This section documents the analytical solutions and computational results for the potential configurations shown in Figure 23.

A. RECTANGULAR BARRIER

The electron reflectivity for a free electron encountering a rectangular barrier is the easiest to solve. The Schroedinger solutions inside the rectangular barrier of Figure 23b are expressable in terms of trigonometric and hyperbolic functions. The electron reflection coefficient, R, for the rectangular barrier model can be stated as follows:

$$R = (R_1^2 + R_2^2)/(R_3^2 + R_4^2), \text{ for } 0 < E < \phi_b \tag{10a}$$

$$R_1 = \left[\sqrt{E(E + \mu + \phi_e)} + (\phi_b - E)\right] \tanh \left[\frac{\sqrt{2m(\phi_b - E)}\, b}{\hbar}\right] \tag{10b}$$

$$R_2 = \sqrt{\phi_b - E}\left[\sqrt{E + \mu + \phi_e} - \sqrt{E}\right] \tag{10c}$$

$$R_3 = \left[\sqrt{E(E + \mu + \phi_e)} - (\phi_b - E)\right] \tanh \left[\frac{\sqrt{2m(\phi_b - E)}\, b}{\hbar}\right] \tag{10d}$$

$$R_4 = \sqrt{\phi_b - E}\left[\sqrt{E + \mu + \phi_e} + \sqrt{E}\right] \tag{10e}$$

$$R = (S_1^2 + S_2^2) / (S_3^2 + S_4^2), \text{ for } E > \phi_b \tag{11a}$$

$$S_1 = \left[\sqrt{E(E + \mu + \phi_e)} - (E - \phi_b)\right] \tan \left[\frac{\sqrt{2m(E - \phi_b)}\, b}{\hbar}\right] \tag{11b}$$

$$S_2 = \sqrt{E - \phi_b}\left[\sqrt{E + \mu + \phi_e} - \sqrt{E}\right] \tag{11c}$$

$$S_3 = \left[\sqrt{E(E + \mu + \phi_e)} + (E - \phi_b)\right] \tan \left[\frac{\sqrt{2m(E - \phi_b)}\, b}{\hbar}\right] \tag{11d}$$

$$S_4 = \left[\sqrt{E - \phi_b}\right]\left[\sqrt{E + \mu + \phi_e} + \sqrt{E}\right] \tag{11e}$$

The foregoing equations are amenable to electronic computation (see program listing in Appendix D) and are analogous to similar phenomena exhibited by thin films interferring with incident light. For example, the minima occur at electron energies corresponding to de Broglie wavelengths ($\lambda = h/p$) which are multiples of twice the barrier thickness. Such spectral structure of electron reflectivity has been experimentally observed.[6]

B. TRIANGULAR BARRIER

For the ramp potential barrier model, the relationship between electron reflectivity and energy can be obtained by means of a series solution of the Schroedinger equation:

$$R = \left| \frac{ik_r \sum_{n=0}^{\infty} A_n b^n + \sum_{n=1}^{\infty} n A_n b^{n-1}}{ik_r \sum_{n=0}^{\infty} A_n b^n - \sum_{n=1}^{\infty} n A_n b^{n-1}} \right|^2 \qquad (12a)$$

$$k_r = \frac{\sqrt{2mE}}{h}, \quad k_1 = \frac{\sqrt{2m(E + \mu + \phi_e)}}{\not{h}} \qquad (12b)$$

$$A_0 = 1, \quad A_1 = -ik_1, \quad A_2 = \frac{-2m(E - \phi_b)}{\not{h}^2} \qquad (12c)$$

$$A_{n+2} = \frac{-2m}{\not{h}^2 (n+1)(n+2)} \left[(E - \phi_b) A_n + \frac{\phi_b}{b} A_{n-1} \right] \qquad (12d)$$

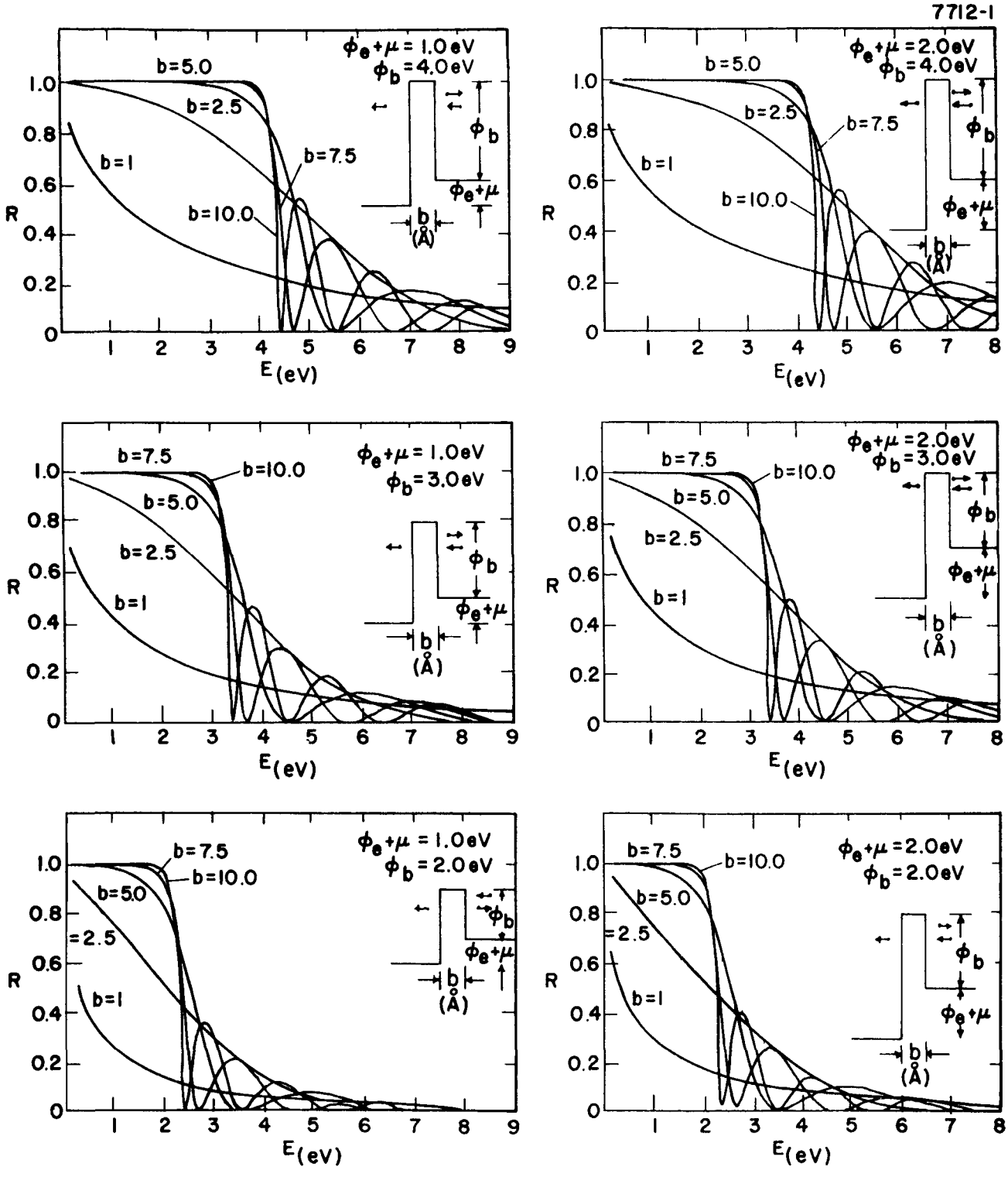

Figure 25. Electron Reflectivity Spectra for Rectangular Energy Barriers (ϕ_e = 0.5 eV).

For large values of barrier thickness, b, the summations in Equation 12a converge very slowly. For such cases, as derived in Appendix B, the wave functions in the barrier region can be expressed in terms of Airy functions or Bessel functions, for which more rapidly converging forms are known. The expression for reflectivity reflection spectra for families of triangular barriers are shown in Figure 26. The values for these curves were calculated from Equation 12a.

C. RECTANGULAR BARRIER WITH IMAGE POTENTIAL

Incorporation of image potential $V(x) = \frac{e^2}{16\pi\epsilon_o x}$ effects on electron reflection involves solutions of the form

$$\frac{h^2}{2m}\frac{d^2\phi}{dx^2} + \frac{e^2}{16\pi\epsilon_o x}\phi = E\phi \qquad (13)$$

Complete algebraic expressions for the solutions to this equation become rather complicated. The correct solution must asymptotically approach traveling waves for $x \to \infty$ in order to be physically meaningful. The MacColl solution[7] for electron reflection in the presence of an image field was analyzed in order to obtain an equation amenable to computer programming. Becuase of the complexity of MacColl's formulas, an analysis of the above equation was performed, resulting in simpler expressions involving confluent hypergeometric functions of the second kind. Comparison with MacColl's solutions showed that the two solutions, derived independently, are identical. Employing the results of the detailed

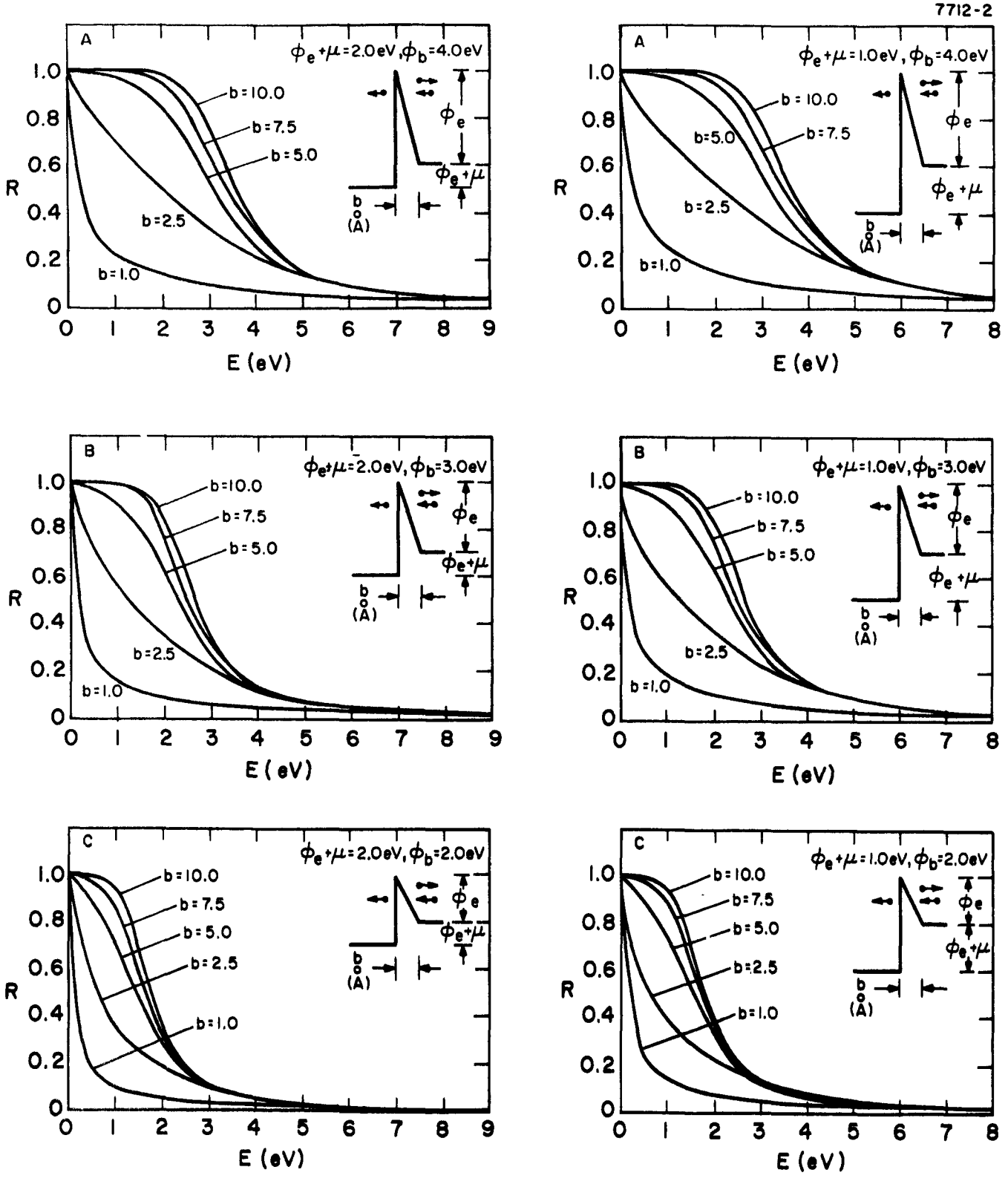

Figure 26. Electron Reflectivity Spectra for Triangular Energy Barriers

analysis for the constituent functions given in the Appendix A, one can obtain the desired reflectivity by the application of Equation 9.

D. TRIANGULAR BARRIER WITH IMAGE POTENTIAL

For the specialized case of a narrow triangular barrier and an image field one can derive a simple expression for reflectivity based upon the analysis used to derive Equation 12a.

$$R = \left| \frac{h_1 f_+(-b) - h_2 f_+'(-b)}{h_1 f_-(-b) - h_2 f_-'(-b)} \right|^2 \qquad (14)$$

where confluent hypergeometics functions for positive and negative traveling waves (see Appendix A).

$$h_1 = \sum_{k=1} kA_k(-b)^{k-1}$$

$$h_2 = \sum_{k=1} A_k(-b)^k$$

A_k - See Equation 12

E. COMPARISONS AMONG REFLECTIVITY SPECTRA

Because of the greater ease of programming and computing, a larger variety of reflectivity curves were made for the cases involving no image potential. Reflectivity spectra for rectangular potential barrier, in the absence of the image potential, are shown in Figure 25. The reflectivity maxima and minima are analogous to similar phenomena exhibited by thin films interfering with light. In fact, such electron reflectivity spectra have been experimentally observed for gold films deposited upon polcrystalline iridium.[6]

For the thinner barriers, tunneling is quite substantial, and the low energy reflectivity increases as the drop $(\phi_e + \mu)$ from the free electron potential increases. For thicker surface barriers (greater than 5 Å), a collection threshold is established by the barrier height and the reflection coefficient is independent of $(\phi_e + \mu)$.

An analogous set of curves for triangular surface barriers is shown in Figure 26. The most evident difference between the reflectivity spectra of the rectangular and triangular barriers is the latter's lack of oscillations. This is not too surprising in view of the less abrupt potential configuration of the triangular barrier. There are a number of similarities, however. For thinner barriers reflectivity increases with $(\phi_e + \mu)$; for thicker barriers the threshold for collection - although not so abrupt as for the rectangular barrier - is still established by barrier height. For all rectangular and triangular barriers studied in the absence of the image potential, the zero energy value of reflectivity is unity - total reflection.

The effect of the addition of the image potential to the above surface barrier models should be considered first in terms of the former's relative strength. The derivations of reflection coefficents for rectangular and triangular surface barriers superimposed with the image potential are given in Appendix C. As shown in Figure 27, the image potential is dramatically stronger for distances of less than 1 Å. MacColl, for his barrierless model, chose to abruptly terminate the image potential at that point where it is equal to the predefined bulk potential.[7] The result is a reduction of the zero-energy reflection coefficient from unity to less than 0.06. One must bear in

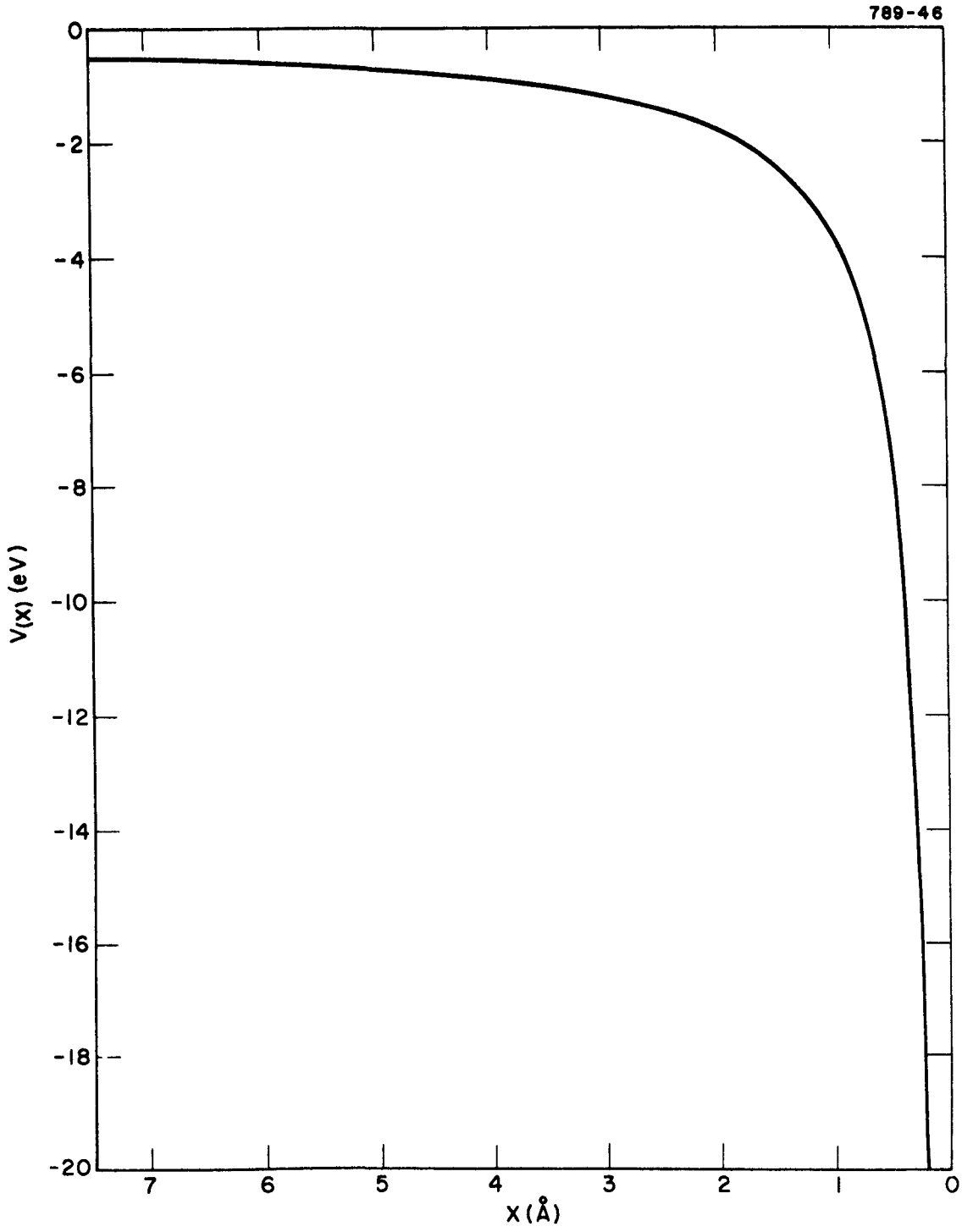

Figure 27. Image Potential: x < 0, Vacuum; x > 0, Metal

mind that this dramatic change results from the smoothing-out of the transition in electron potential brought about by the presence of the image potential. The introduction of a surface barrier, of course, breaks up this transition. One must also consider the relative magnitudes between the kinetic and potential energies of the incident electron. For the barrierless models if kinetic energy is comparable to or greater than the depth of the potential well, which represents the collecting material, there is practically no difference for electron reflectivity in the absence or presence of an image potential.

The reflectivity spectra for the rectangular barrier model with the image potential, shown in Figure 28, may be compared to the reflectivity spectra for the rectangular barrier without the image potential given in Figure 25. The values of barrier height and potential well depth were chosen on the basis of the 1.6 eV collector work function which has been typically measured in the past and on the basis of value of conduction band minimum obtained by photo-electron emission measurements on tungsten.[8] In view of the foregoing discussion, it is not surprising that for sufficiently large barrier widths the image potential has a negligible effect upon the reflectivity spectrum. At a 1 Å barrier width, however, the image potential brings about a reduction of the zero energy value of reflectivity from unity to 0.41. For the mid-ranges of barrier width, the image potential reduces electron reflectivity at low energies and increases it at higher energies. The physical reason for this behavior is not clear.

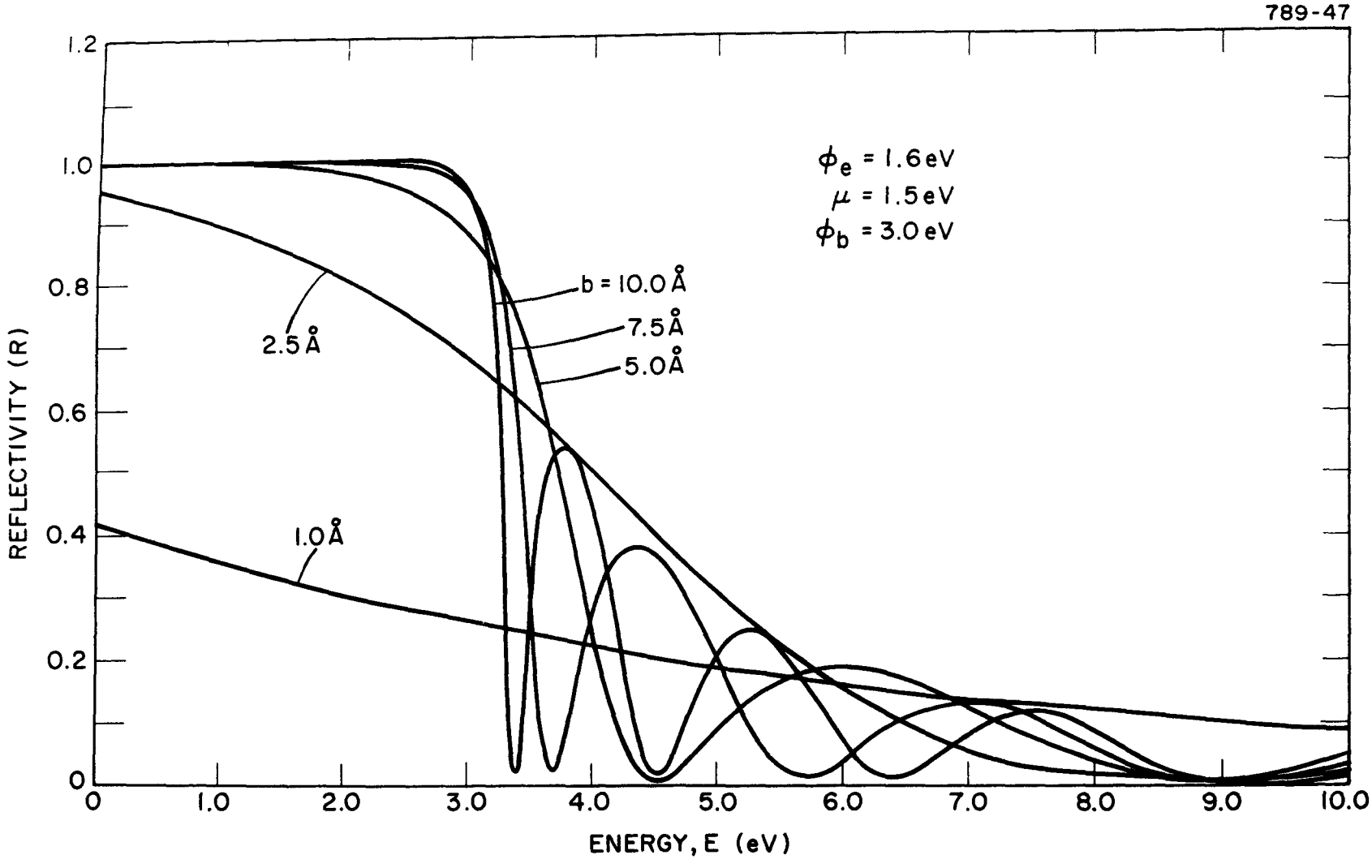

Figure 28. Electron Reflectivities for a Rectangular Barrier with Image Potential

A similar comparison of the triangular surface barrier models can be made by inspecting Figures 26 and 29. Again, for barrier thicknesses greater than about 5 Å, the image potential has negligible effect upon reflectivity spectra. The effect of reducing the reflection coefficient for thin barriers is more dramatic, however. The zero energy reflectivity for a 1 Å thick triangular barrier is reduced by the image potential from unity to 0.11.

The above two models ignore the superposition of the barrier and image potentials. It seems highly unlikely that the image potential would be completely screened out in the surface barrier. Figure 30 shows the effects of such a superposition. The basis for the parameter selection has already been mentioned. The barrier depression results in a pronounced lowering of reflection coefficient. The sharp minimina in these curves have no analogues in the positive barrier cases studied. It is interesting to note that the de Broglie wavelengths corresponding to the sharp reflectivity minima are of the order of the surface barrier thickness.

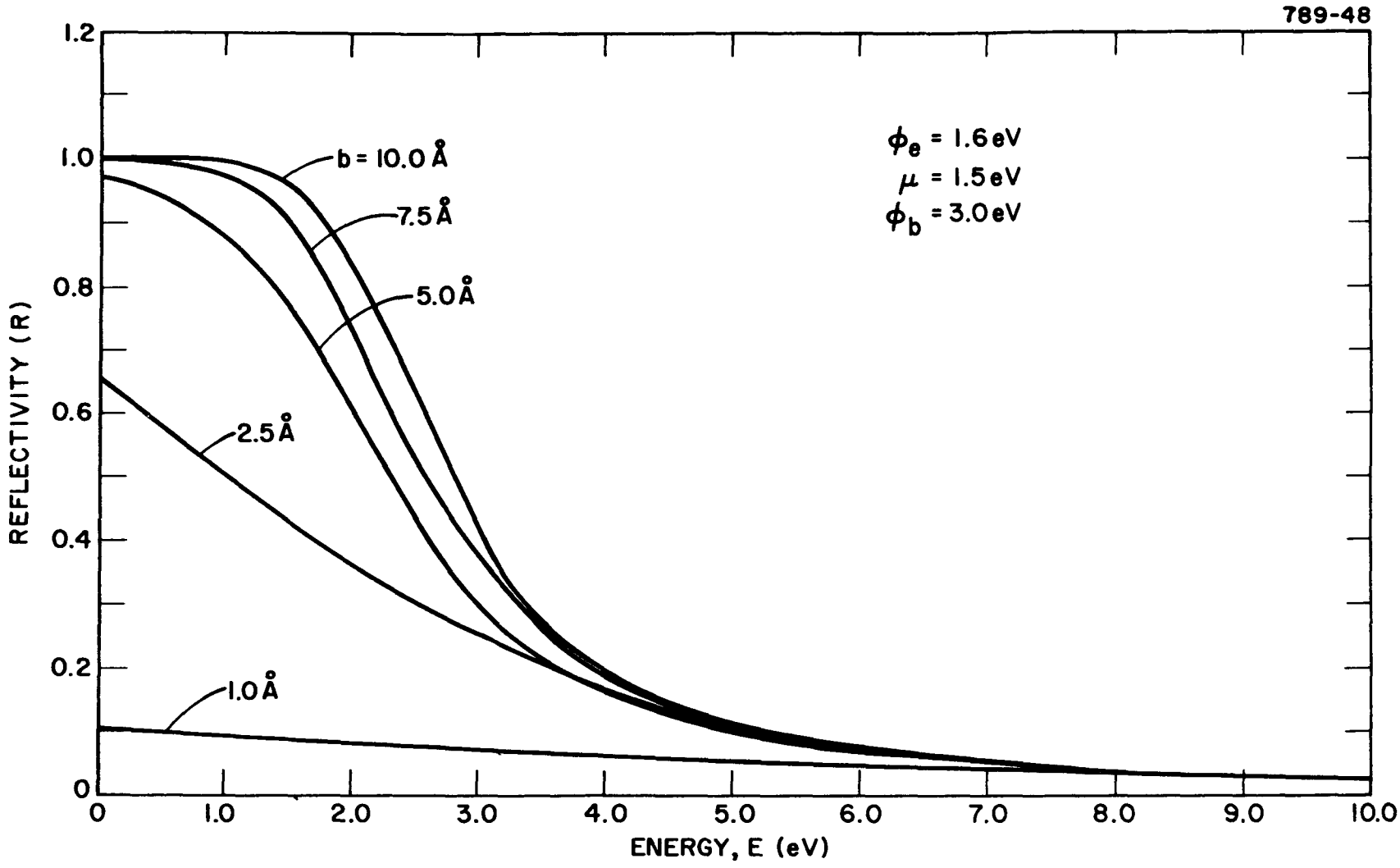

Figure 29. Electron Reflectivities for a Triangular Barrier with Image Potential

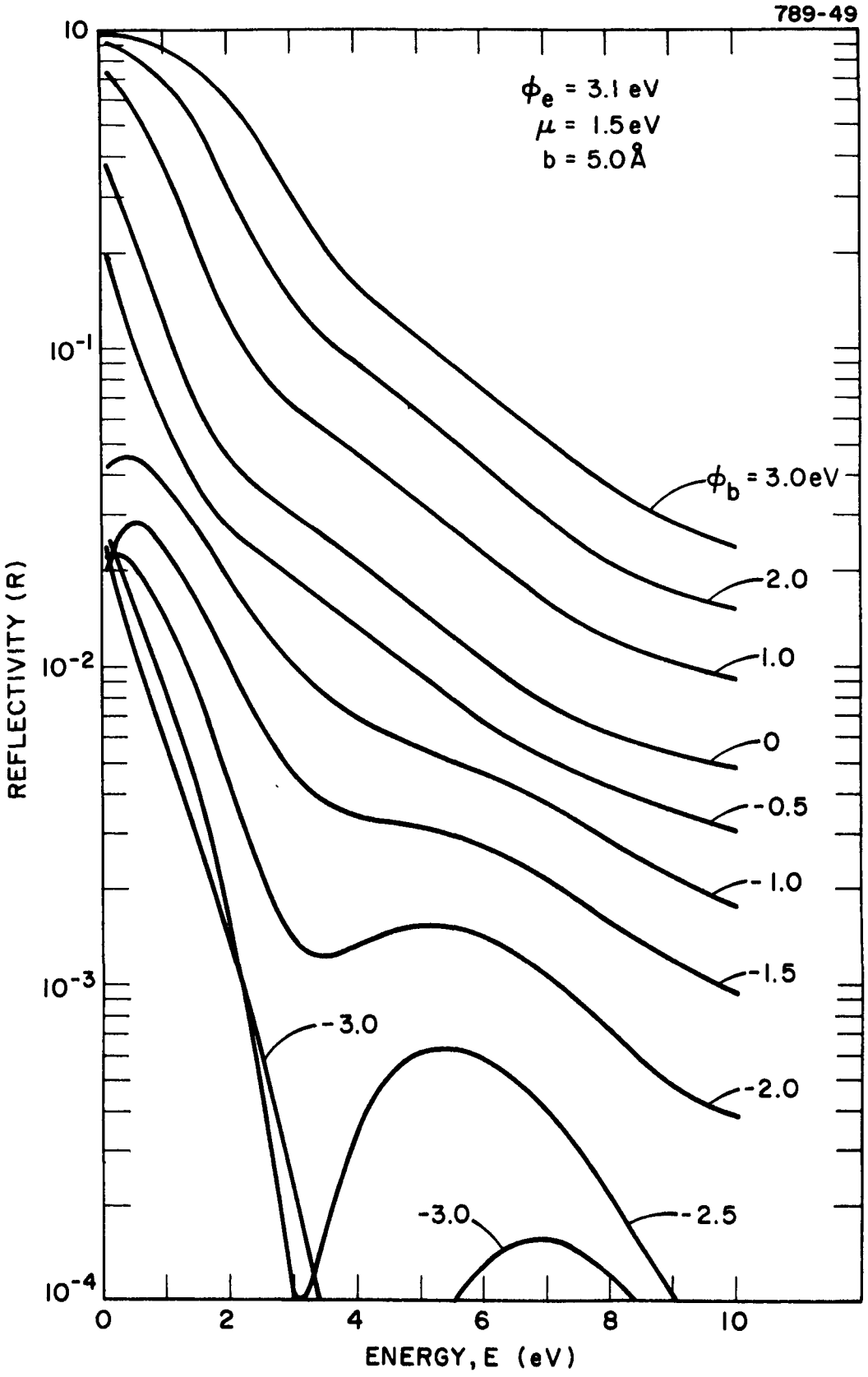

Figure 30. Reflectivity Spectra for Image Potential - Triangular Surface Barrier for Various Barrier Heights

BLANK

V. DISCUSSION

As indicated by theoretical calculations and demonstrated by experimental results, electron reflectivity at thermal energies such as those encountered in a thermionic converter is of substantial magnitude. Rectangular potential barriers have a more pronounced effect upon electron reflectivity.

The more narrow the surface barrier, the more pronounced is the effect of the image potential. For surface barriers greater than 10 Å, the image potential has practically no effect. Tunneling through the surface barrier is appreciable only for barriers less than 5 Å thick (i.e., about one monolayer). If imaging effects inside of a thicker (> 5 Å) barrier are ignored, the low work functions (< 1.3 eV) observed for surface composites of 30 to 100 Å thick must occur because the composite itself is a low work function material. If it has its own surface barrier, the latter must be of the order of a monolayer thick.

The analyses herein gave no consideration for electron spin-spin interactions which are appreciable for an electron gas inside a metal. Theorectical calculations based upon jellium models[9] and incorporating exchange and correlation potentials[10] have been made for electron interaction with a termination of the metal.

Although converter electrode materials like tungsten and molybdenum are not as jellium-like as the alkali metals, it is worth while considering surface-barrier-on-jellium calculations simply because they do provide a means of determining the effect of electron-electron interactions on electron reflectivity at the collector of a

thermionic converter.

The surface barrier is established by the net combination of positive and negative charge distributions which comprise the surface composite layer. The surface density formalism of Hohenberg and Kohn[11] - a method for determining the minimum energy charge distribution is possible means of determing the net distribution (and, hence, the surface barrier potential).

Surface composites of the order of 30 to 100 Å thick are three dimensional materials. Hence, considerations should be made for the effect of solid state transport phenomena, e.g., phonon scattering, upon electron reflectivity. Plausible qualitative explanations of FERP spectra in terms of semiconductor/insulator-like phonon scattering have been considered.[12] Hence, this subject deserves further study.

VI. REFERENCES

1. C. L. Balestra and F. N. Huffman, 1975 Thermionic Specialists Meeting, Eindhoven, Netherlands (1975).

2. R. W. Strayer, W. Mackie, and L. W. Swanson, Work Function Measurement by the Field Emission Retarding Potential Method, Surface Sci. 34, 225 (1973).

3. F. Rufeh and D. Lieb, "The Dependence of the Volt-Ampere Characteristics on Collector Temperature, "IEEE Conf. Record 69 C 51-ED 1969 Thermionic Conversion Specialist Conf. (Carmel) p. 237 (October 1969).

4. K. Ritz and J. Bohdansky, "Collector Heat Dissipation in a Variable Spacing Diode, "Proc. 1975 Thermionic Conversion Specialists Meeting (Eindhoven), p. 221 (September 1974).

5. F. N. Huffman et al. "High Efficiency Thermionic Converter Studies," Thermo Electron Corporation TE 4202-12-77, p 55 (1977).

6. R. E. Thomas, "Interference Effects in the Reflection of Low-Energy Electrons for Thin Films of Au on Ir, " J. Appl. Phys. 41, 5330 (1970).

7. L. A. MacColl, "Numerical Calculations of Reflection of Electrons by Metals," Phys. Rev. 56, 699 (1939).

8. I. Petroff and C. R. Viswanathan, "Calculation of the Photoelectric Emission from Tungsten, Tantalum, and Molybdenum," Phys. Rev. B, 4, 799 (1971)

9. G. D. Mahan, Phys. Rev. B 12, 5585 (1975).

10. D. C. Langreth and J. P. Perdew, "Exchange-Correlation Energy of a Metallic Surface: Wave-Vector Analysis," Phys. Rev. B 15, 2884 (1977).

11. N. D. Lang, "The Density Functional Formalism and the Electronic Structure of Metal Surfaces," Solid State Physics 28, 225 (1973).

12. W. E. Spicer - private communication

APPENDIX A
SOLUTIONS OF THE SCHROEDINGER EQUATION FOR AN IMAGE POTENTIAL

The one-dimensional Schroedinger equation for an image potential in the region $x < 0$, with the mirror plane at $x = 0$, can be stated as

$$\frac{-\hbar^2}{2m}\frac{d^2\phi(x)}{dx^2} + \frac{e^2}{16\mu\epsilon_o x}\phi(x) = E\phi(x) \qquad \text{(A1)}$$

Traveling wave-like solutions can be obtained by transforming to a form of Whittaker's equation:[1]

$$\xi \equiv I\ i\eta x, \quad \eta \equiv 2\sqrt{2mE}/\hbar \qquad \text{(A2a)}$$

$$\lambda \equiv \mp i\sigma, \quad \sigma \equiv \sqrt{2m}\ e^2/32\hbar\mu\epsilon_o\sqrt{E} \qquad \text{(A2b)}$$

$$\frac{d^2\phi}{d\xi^2} + \left(\frac{\lambda}{\xi} - \frac{1}{4}\right)\phi = 0, \text{ Whittaker's equation} \qquad \text{(A2c)}$$

$$\phi(\xi) = e^{-\xi/2}U(1-\lambda, 2, \xi), \qquad \text{(A2d)}$$

where $U(1-\lambda, 2, \xi)$ is a confluent hypergeometric function of the second kind.[2] The traveling wave-like nature of this solution can be verified in terms of the asymptotic expansion for $U(1-\lambda, 2, \xi)$ as $|\xi|$ approaches indinity.[3]

$$\phi(\xi) \xrightarrow[\xi \to \infty]{} \xi^{\lambda} e^{-\xi/2} = (\mp i\eta x)^{\mp i\sigma} e^{\mp i\eta x/2} \qquad \text{(A3)}$$
$$= e^{\pi/2} e^{\pm ikx}, \quad k = \sqrt{2mE}/h$$

For $\xi = -i\eta x$ and $\lambda = -i\sigma$ the solution for large negative values of x behaves as a de Broglie wave, with wave number k, traveling in the

positive direction toward the minor plane at x = 0. For $\xi = i\,x$ and $\lambda = i\sigma$ we have the complementary reflected wave. As in the case for traveling plane waves, the image potential analogues are complex conjugates of each other.

By means of recurrence relationships,[4] $\phi(\xi)$ and its first derivative, both necessary for computing the reflection coefficient, can be transformed into forms more readily programmable:

$$\phi(\xi) = e^{-\xi/2}\,[\lambda\, U(1-\lambda,\ 1,\ \xi) + U(-\lambda,\ 1,\ \xi)] \tag{A4a}$$

$$\phi'(\xi) = (e^{-\xi/2}/2)\,[\lambda\, U(1-\lambda,\ 1,\ \xi) - U(-\lambda,\ 1,\ \xi)] \tag{A4b}$$

$$U(-\lambda,\ 1,\ \xi) = \frac{-1}{\Gamma(-\lambda)}\left[M(-\lambda,\ 1,\ \xi)\ln\xi + \sum_{r=0}^{\infty}\frac{(-\lambda)_r\,\xi^r}{(r!)^2}\cdot\psi(-\lambda) + S_r(\lambda)\right] \tag{A4c}$$

$$U(1-\lambda,\ 1,\ \xi) = \frac{-1}{(1-\lambda)\,\Gamma(-\lambda)}\ M(1-\lambda,\ 1,\ \xi)\ln\xi + \sum_{r=0}^{\infty}\frac{(1-\lambda)_r\,\xi^r}{(r!)^2}\left(\psi(-\lambda) + S_r(\ ) + \frac{1}{(r-\lambda)}\right) \tag{A4d}$$

$$M(a,\ b,\ z) = 1 + \frac{az}{b} + \frac{(a)_2}{b} + \cdots \frac{(a)_n z^n}{(b)_n n!} + \cdots \tag{A4e}$$

$$(a)_r \equiv a(1+a)\,(2+a)\cdots(r-1+a),\quad (a)_0 \equiv 1 \tag{A4f}$$

$$S_r(\lambda) \equiv 2\gamma + \sum_{L=1}^{\infty}\frac{1}{(r-L-\lambda)} - \frac{2}{(r-L+1)} \tag{A4g}$$

Because $U(-\lambda, 1, \xi)$ and $U(1-\lambda, 1, \xi)$ are both common to the numerator and denominator of the expression for reflection coefficient, the gamma function $\Gamma(-\lambda)$ factors out and this can be ignored. Summation formulas and asymptotic expansions for $M(-\lambda, 1, \xi)$ and $M(1-\lambda, 1, \xi)$, the confluent hypergeometric functions of the first kind,[5] and $\psi(-\lambda)$ the digamma function,[6] are readily available. Equations were verified by their duplication of MacColl's results by using the barrier-free model as a limiting case.

REFERENCES

(1) M. Abramowitz and S. Stegren, Handbook of Mathmatical Functions (Dover Publications, Inc., New York, 1965), p. 505.

(2) Ibid, p. 504.

(3) Ibid, p. 508.

(4) Ibid, pp. 507 and 508.

(5) Ibid, pp. 504 and 508.

(6) Ibid, pp. 258 and 259.

APPENDIX B

B. 1 GENERALIZED SOLUTION OF THE SCHROEDINGER EQUATION FOR A RAMP POTENTIAL

The Schroedinger equation inside of a triangular surface barrier ($V = Hx + \phi_b$) can be stated as,

$$\frac{\hbar^2}{2m}\frac{d^2\phi(x)}{dx^2} + (Hx + \phi_b)\,\phi(x) = E\phi(x) \tag{B1}$$

By substituting for $z = -H^{-2/3}\left(\frac{2m}{\hbar^2}\right)^{1/3}[E - \phi_b - Hx]$. (B2)

one obtains the equation

$$\frac{d^2\phi}{dz^2} - z\phi = O \tag{B3}$$

whose solutions can be stated in terms of Airy[1] and modified Bessel[2] functions

$$\phi = CAi(z(x)) + DBi(z(x)) \tag{B4}$$

$$Ai(z) = \frac{1}{3}\sqrt{z}\,[I_{-1/3}(\tfrac{2}{3}z^{3/2}) - I_{1/3}(\tfrac{2}{3}z^{3/2})]$$
$$= \pi^{-1}(\sqrt{z}/3)\,K_{1/3}(\tfrac{2}{3}z^{3/2}) \tag{B5a}$$

$$Ai'(z) = \frac{1}{3}z\,[I_{2/3}(\tfrac{2}{3}z^{3/2}) - I_{-2/3}(\tfrac{2}{3}z^{3/2})]$$
$$= -\pi^{-1}(z/\sqrt{3})\,K_{2/3}(\tfrac{2}{3}z^{2/3}) \tag{B5b}$$

$$Bi(z) = (\sqrt{z}/3)\,[I_{-1/3}(\tfrac{2}{3}z^{3/2}) + I_{1/3}(\tfrac{2}{3}z^{3/2})] \tag{B5c}$$

$$Bi'(z) = (z/\sqrt{3})\,[I_{-2/3}(\tfrac{2}{3}z^{3/2}) + I_{2/3}(\tfrac{2}{3}z^{3/2})] \qquad \text{(B5d)}$$

For large values of z(x) asymptotic expansions[3, 4] are readily available, both for the functions and their first derivatives.

REFERENCES

(1) M. Abramowitz and S. Stegren, Handbook of Mathematical Functions, (Dover Publications, Inc., New York, 1965), p. 446.

(2) Ibid., p. 447.

(3) Ibid., pp. 448 and 449.

(4) Ibid., pp. 377 and 378.

APPENDIX C

ELECTRON REFLECTION FROM A SURFACE BARRIER IN THE PRESENCE OF AN IMAGE POTENTIAL

By incorporating the rectangular barrier and image potential solutions into the generalized formula for reflection coefficient (Equation 9), reflectivity expressions are derived as shown in Figure C1.

The expression for reflectivity coefficient for an electron traveling through an imaging field toward a triangular barrier can be derived in a similar fashion by applying the ramp potential solutions in place of those for a rectangular barrier (see Figure C2).

The ramp slope H is determined by matching the ramp to the image potential at their point of intersection.

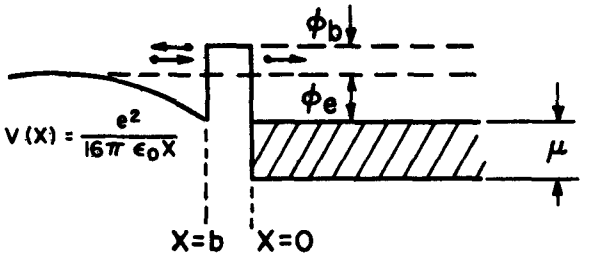

$$\alpha = \frac{\sqrt{2m}\, e^{3/2}}{8\pi\hbar x} = 3.6886 \qquad \beta = \frac{\sqrt{2me}}{\hbar}\, 10^{-10} = 0.51231$$

$$U_1 = U(i\alpha/4\sqrt{E}, 1; 2i\beta\sqrt{E}\, b) \qquad b \text{ in } \mathring{A}$$

$$U_2 = U(1 + i\alpha/4\sqrt{E}, 1; 2i\beta\sqrt{E}\, b) \qquad E,\ \phi_e,\ \mu,\ \phi_b \text{ in eV}$$

$$E < \phi_b,\ R = \frac{\left| \left(U_1 - \frac{i\alpha}{4\sqrt{E}} U_2\right)\left[-\sqrt{\phi_b - E}\tanh(\beta\sqrt{\phi_b - E}\, b) + \sqrt{E + \phi_e + \mu}\right] - i\sqrt{E}\left(U_1 + \frac{i\alpha}{4\sqrt{E}} U_2\right)\left[1 - \sqrt{\frac{E + \phi_e + \mu}{\phi_b - E}}\tanh(\beta\sqrt{\phi_b - E}\, b)\right]\right|^2}{\left| -i\sqrt{E}\left(U_1^* - \frac{i\alpha}{4E} U_2^*\right)\left[1 - \frac{\sqrt{E + \phi_e + \mu}}{\sqrt{\phi_b - E}}\tanh(\beta\sqrt{\phi_b - E}\, b)\right] - \left(U_1^* + \frac{i\alpha}{4\sqrt{E}} U_2^*\right)\left[-\sqrt{\phi_b - E}\tanh(\beta\sqrt{\phi_b - E}\, b) + \sqrt{E + \phi_e + \mu}\right]\right|^2}$$

$$E > \phi_b,\ R = \frac{\left| \left(U_1 - \frac{i\alpha}{4\sqrt{E}} U_2\right)\left[\sqrt{E - \phi_b}\tan(\beta\sqrt{E - \phi_b}\, b) + \sqrt{E + \phi_e + \mu}\right] - i\sqrt{E}\left(U_1 + \frac{i\alpha}{4\sqrt{E}} U_2\right)\left[\left(1 - \sqrt{\frac{E + \phi_e + \mu}{E - \phi_b}}\tan(\beta\sqrt{E - \phi_b}\, b)\right)\right]\right|^2}{\left| -i\sqrt{E}\left(U_1^* - \frac{i\alpha}{4\sqrt{E}} U_2^*\right)\left[1 - \sqrt{\frac{E + \phi_e + \mu}{E - \phi_b}}\tan(\beta\sqrt{E - \phi_b}\, b)\right] - \left(U_1^* + \frac{i\alpha}{4\sqrt{E}} U_2^*\right)\left[\sqrt{E - \phi_b}\tan(\beta\sqrt{E - \phi_b}\, b) + \sqrt{E + \phi_e + \mu}\right]\right|^2}$$

Figure C.1 Reflectivity Coefficient Expressions for Rectangular Barrier in the Presence of an Image Potential

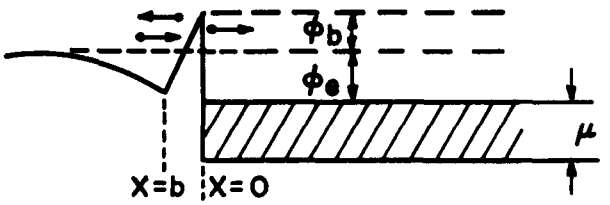

$$g \equiv U_1 - \frac{i\alpha}{4\sqrt{E}} U_2, \quad g' \equiv i\beta\sqrt{E}\, U_1 + \frac{i\alpha}{4\sqrt{E}} U_2$$

$$z_o \equiv z(x=0) = \frac{-0.64014\,(E-\phi_b)}{\left(\frac{3.5999}{b^2} + \frac{\phi_b}{b}\right)^{3/2}}$$

$$z' = 0.64014\left(\frac{3.5999}{b^2} + \frac{\phi_b}{b}\right)^{1/3}$$

$$z_b = z(x=b) = \left[\frac{-0.64014}{\left(\frac{3.5999}{b^2} + \frac{\phi_b}{b}\right)^{3/2}}\right]\left[E - 2\phi_b - \frac{3.5999}{b}\right]$$

$$f = \left[B'i(z_o)\; z' - i\,Bi(z_o)\;\beta\sqrt{E+\phi_e+\mu}\right] Ai(z_b) + \left[i\,Ai(z_o)\;\beta\sqrt{E+\phi_e+\mu} - A'i(z_o)\; z'\right] Bi(z_b)$$

$$f' = \left[Bi'(z_o)\; z' - i\,Bi(z_o)\;\beta\sqrt{E+\phi_e+\mu}\right] A'i(z_b)\; z' + \left[i\,Ai(z_o)\,\beta\sqrt{E+\phi_e+\mu} - A'i(z_o)\; z'\right] B'i(z_b)\; z'$$

$$R = \left|g f' - g' f\right|^2 \Big/ \left|(g')^* f - g^* f\right|^2$$

Figure C.2 Reflectivity Coefficient Expression for a Triangular Barrier in the Presence of an Image Potential

APPENDIX D

Listing of Computer Programs

D-1. BASIC Program for Rectangular Barrier Reflectivity in Absence of Image Potential*

```
10 REMARK PROGRAM TO COMPUTE REFLECTION COEFFICIENT
20 PRINT "WELL DEPTH W";
25 INPUT W
30 PRINT "BARRIER HEIGHT WB";
35 INPUT W1
40 PRINT "BARRIER WIDTH B";
45 INPUT B
50 PRINT
60 PRINT
70 PRINT "ENERGY E", "REFLECTION"
80 PRINT
90 DEF FNA(X)=(EXP(X)-EXP(-X))/(EXP(X)+EXP(-X))
100 DEF FNB(X)=SIN(X)/COS(X)
110 LET E=W
120 LET E=E+.1
130 LET K1=SQR(E-W)
140 LET K2=SQR(ABS(W+W1-E))
150 LET K3=SQR(E)
160 IF E>=(W+W1) GO TO 230
170 LET R1=(K1*K3+K2*K2)*FNA(.51231*K2*B)
180 LET R2=K2*(K1-K3)
190 LET R3=(K1*K3-K2*K2)*FNA(.51231*K2*B)
200 LET R4=K2*(K1+K3)
210 LET R=(R1*R1+R2*R2)/(R3*R3+R4*R4)
220 PRINT E,R
225 GOTO 120
230 LET S1=K2*(K1-K3)
240 LET S2=(K2*K2-K1*K3)*FNB(.51231*K2*B)
250 LET S3=K2*(K1+K3)
260 LET S4=(K2*K2+K1*K3)*FNB(.51231*K2*B)
270 LET S=(S1*S1+S2*S2)/(S3*S3+S4*S4)
280 PRINT E,S
290 IF E<=10. GO TO 120
300 END
READY
```

* For E in this program substitute the term $E + \rho_e + \mu$ as difined in the text of this report. For well depth W substitute $\rho_e + \mu$.

D-2. FORTRAN Program for Triangular Barrier Reflectivity in the Absence of Image Potential*

```
0001            INTEGER W,WB,I,L
0002            REAL C,B,E,G,H,FL,FR
0003            COMPLEX A0,A1,A2,AN,S1,S2,AP1,AP2,Z
0004            C= 2624664
0005      10    FORMAT (///11X, W 19X, WB 8X, B'/)
0006            PRINT 20, W, WB, B
0007      20    FORMAT (2I13,G13 6//)
0008            PRINT 30
0009      30    FORMAT (  E                        R /)
0010            W=1
0011            WB=4
0012            B=5
0013            E =W
0014      70    E=E+ 1
0015            G=C*(E-W-WB)
0016            H=C*WB/B
0017            FL=SQRT(C*E)
0018            FR=SQRT(C*(E-W))
0019            PRINT 40, G,H,FL,FR
0020      40    FORMAT(  G,H,FL,FR= ,4G13 6)
0021            A0=CMPLX(1 ,0)
0022            A1=CMPLX(0,-1 )*FL*A0
0023            A2=-G*A0/Z
0024            S1=A0+A1*B+A2*B**2
0025            S2=A1+2 *A2*B
0026            PRINT 50, S1,S2
0027      50    FORMAT ( S1,S2= ,4G13 6)
0028            L=2
0029      80    L=L+1
0030            AN=-(G*A1+H*A0)/(L*(L-1))
0031            A0=A1
0032            A1=AN
0033            AP1=AN*B**L
0034            AP2 L*AN*B**(L-1)
0035            PRINT 60, AP1,AP2
0036      60    FORMAT (  AP1,AP2=  ,4G13 6)
0037            S1=S1+AP1
0038            S2=S2+AP2
0039            PRINT 50, S1,S2
0040            IF (L  LT  21) GO TO 80
0041            Z=(CMPLX(0,1 )*FR*S1+S2)/(CMPLX(0,1 )*FR*S1-S2)
0042            R=Z*CONJG(Z)
0043            PRINT 65  Z,R
0044      65    FORMAT (  Z,R= , 3G13 6)
0045            PRINT 90, E,R
0046      90    FORMAT (2F20 10)
0047            IF (E  LT  10 0) GO TO 70
0048      100   CONTINUE
0049            END
```

* For E in this program substitute the term $E + \mu_e + \mu$ as defined in the text of this report for well depth W substitute $\mu_e + \mu$.

D-3. FORTRAN Programs for Calculations Involving the Image Potential

For PHIE in these programs subsitute $\mu_e + \mu$ as defined in the text of this report.

a) Confluent Hypergeometric Function

b) Main Program for Company Reflection Coefficient for Rectangular of Triangular Barriers in the Presence of the Image Potential

c) Airy Function of a Computer Argument

d) Comma Functions of Complex Argument and D:Gamma

e) Subroutine for Computing Airy Function of a Complex Argument

Figure D-3a. Confluent Hypergeometric Function

```
!COPY UF ON ME
      SUBROUTINE U!A,B,Z,U,NF',NF'!
      COMMON  BLOCK2 CHECK,CHECK1,CHECK2,CHECKU
      COMMON  BLOCK4 ULIM
      COMPLEX FA,FB,FC,FZ
      COMPLEX U,A,Z,U',Y',GAMMA,CONF,PSI,AA,BB,CC
      LOGICAL MORE,CHECK,CHECK1,CHECK2,CHECKU
      DATA CON!'1.E-9
      DATA P/.5772156649015329
 1000 FORMAT(I4,4G16.9,4X,2G16.9)
 2000 FORMAT(I6,4G16.9)
      B = FLOAT(NB)
      AA = A
      C = 1.
      IF(CABS(Z) .GT. ULIM) GO TO 300
      NF' = 1
      FA = PSI(AA)
      IF(CHECKU) OUTPUT FA
      FC = -P
      FB = FC
      IF(NB .EQ. 2) FB = FC + 1.
      FZ = CLOG(Z)
      U = FZ + FA - FC - FB
      ' = 1.
      DO 100 I = 1,100000
      ' = '*(A+I-1.)*Z /(B+I-1.)*I
      FA = FA+1. AA=FB = FB+1. B=FC  = FC+1. C
      AA = AA+1.=B  = B+1.=C    = C+1.
      Y = '*(FZ + FA - FC - FB)
      U = U + Y
      IF(CHECKU .AND. I .GT. 1994) PRINT 1000,I,',U,Y
      IF(CABS(Y) .LT. CON!) GO TO 200
  100 CONTINUE
      OUTPUT ' FUNCTION U DIVERGE'
      OUTPUT I,',U,FA,FB,FC,FZ,'
  200 U = U*(-1.)**NB) GAMMA(A-NB+1.,NF')
      IF(CHECKU) OUTPUT I,',U,FA,FB,FC,FZ
      IF NB .EQ. 1) RETURN
      U = U + Z GAMMA A,NF')
      RETURN
  300 U = 1.0= Y = 1.
      BB = 1.+AA-B
      DO 400 I = 1,2000
      FZ = '
      ' = -Y'*AA*BB /I*Z)
      AA = AA+1.
      BB = BB+1.
      U = U + Y
      IF(CHECKU .AND. I .GT. 1994) PRINT 2000,I,U,Y
      IF(CABS(Y) .LT. CON!) GO TO 500
      IF(CABS(FZ+Y) .LT. CON!) GO TO 500
  400 CONTINUE
      OUTPUT I,U,Y,AA,BB,Z,CABS(Z),ULIM
  500 U = U*(Z** -A))
      AA = Z**(-A)
      IF(CHECKU) PRINT 2000,I,U,AA
      NFX = 2; NFY = 0
      RETURN
      END
```

Figure D-3b. Main Program for Company Reflection Coefficient for Rectangular Triangular Barriers in the Presence of the Image Potential

```
ICOPY TRIF ON HE
      COMMON /BLOCK1/ALPHA,PHIB,PHIE,E,H,DIV,L
      COMMON /BLOCK2/CHECK,CHECK1,CHECK2,CHECKU
      COMMON /BLOCK3/CIV
      COMMON /BLOCK4/ULIM
      COMPLEX U,U1,U2,FX,SX,CFX,CSX,F,FP,F2,F2P,R
      COMPLEX A1,A2,C1,C2,Z,YY,ZZ
      LOGICAL MORE,CHECK,CHECK1,CHECK2,CHECKU
      DATA ALPHA,SIGMA,DIV,CIV,ULIM/.51178749,.92121749,2.0,22.,24./
      DATA MORE,CHECK,CHECK1,CHECK2,CHECKU/T,F,F,F,F/
      NAMELIST
      INPUT
      READ 1000,ES,EN,DE
      READ 1000,PHIBS,PHIBN,DPHIB
      READ 1000,PHIES,PHIEN,DPHIE
      READ 1000,XBS,XBN,DXB
   10 PRINT 4000
      DO 100 PHIB = PHIBS,PHIBN,DPHIB
      DO 100 PHIE = PHIES,PHIEN,DPHIE
      DO 100 XB = XBS,XBN,DXB
      XBM = -XB
      DO 100 E = ES,EN,DE
      CALL F(F2,F2P,XBM,NF3,NF4)
      IF(CHECK) OUTPUT F2,F2P
      SI = SIGMA/SQRT(E)
      AL = ALPHA*SQRT(E)
      BETA = 2.*AL
      A1 = CMPLX(0.,SI)
      A2 = 1. + A1
      C1 = CMPLX(0.,-BETA*XBM)
      C2 = CMPLX(0.,AL)
      CALL U(A1,1,C1,U1,NF1,NF5)
      CALL U(A2,1,C1,U2,NF2,NF6)
      IF(CHECK)OUTPUT A1,C1,U1,U2
      FX = U1 - A1*U2
      SX = C2*U1 - AL*SI*U2
      CFX = CONJG(FX)
      CSX = CONJG(SX)
      IF(CHECK) OUTPUT FX,SX,CFX,CSX
      R = F2P*FX - F2*SX
      Z = F2*CSX - F2P*CFX
      IF(CHECK) OUTPUT R,Z
      R = R/Z
      R2 = REAL(R*CONJG(R))
      PRINT 2000,E,PHIB,PHIE,XBM,H,R2,NF1,NF5,NF2,NF6,NF3,NF4
```

```
  100 CONTINUE
      IF(.NOT. MORE) STOP
      INPUT (10)
      GO TO 10
 1000 FORMAT(10F)
 2000 FORMAT(1X,3F8.3,F8.2,2G12.4,2X,6I1)
 3000 FORMAT(1X,4G18.10)
 4000 FORMAT(/T7,'E',T13,'PHIB',T21,'PHIE',T30,'XB',T39,'H',
     AT51,'R',T60,'CHECK')
 9000 STOP
      END

!OFF

CPU = .1138 CON= 00:10:00 INT = 9 CHG = 0
```

Figure D-3c. Airy Function of a Computer Argument

```
!DELETE MAE
.. 1 FILES DELETED, 17 GRANULES

!COPY IVR ON ME
      FUNCTION IV(V,Z,NF)
      REAL IV
      COMMON  BLOCK2 CHECK,CHECK1,CHECK2,CHECKV
      COMMON  BLOCK3 CIV
      COMPLEX VI,GAMMA,GA
      LOGICAL CHECK,CHECK1,CHECK2,CHECKV
      DATA PI2 6.283185308
      DATA PI,PI5 3.141592653589,1.570796326795/
      DATA CONV 1.E-12
 1000 FORMAT(I5,G16.7)
      IF(CHECK1) OUTPUT '  IVR'
X     IF(ABS(Z)  .GT. CIV)  GO TO 200
      NF = 1
      VI = V+1.
      GA = GAMMA(VI,NF)
      X = 2*Z +.
      IF(Z .LT. 0.0) X = -X
      Y = 1.; S = Y
      DO 100 I =1,2000
      S = S*X/(I*(V+I))
      Y = Y + S
      IF(ABS(S)  .LT. CONV) GO TO 150
  100 CONTINUE
      OUTPUT ' I DIVERGE'
      OUTPUT I,S,Y,GA
  150 IV = (ABS(Z) 2.)**V*Y REAL(GA)
      RETURN
  200 IF(Z .LT. 0.0) GO TO 400
      NF = 2
      U = 4.*V*V
      X = 1.; S = X; Y = 1.; SY = Y
      DO 250 I = 1,1000
      AN =  U-(2*I-1)**2)/(I*8.*Z)
      S = -S*AN; SY = SY*AN
      Y = Y + S; Y = Y + SY
      IF(ABS(SY)  .LT. CONV)  GO TO 300
  250 CONTINUE
      OUTPUT ' I DIVERGE'
      OUTPUT I,S,Y,AN
  300 IV = (E**PI)(V) SQRT(PI2*Z))*Y
      IF(CHECK1) OUTPUT Y,Y,IV
      IF(V .GT. 0.0) RETURN
      YK = YK*SQRT(PI5/Z)*EXP(-Z)
      IV = IV + YK*SIN(V*PI)/PI5
      IF(CHECK1) OUTPUT YK,IV
      RETURN
```

```
400 ZP = -Z
    IU = SQRT(4./(PI3*CP(1)*COS(CP-(1)*PI2 4. - (PI2 0.(
    NF = 3
    RETURN
    END
    FUNCTION FA(AI,BI,AIP,BIP,'(
    DATA C1,C2,CONV /.3507280530878(7,.2588194037928007,1.E-6
    F = 1.; FP = 0.0; G = (; GP = 1.
    SA = 1.; SB = (; (0 = (*(*(
    DO 100 I = 1,1000
    I1 = (I*3-2(; I2 = I1+1; I3 = I1*(I1+1(* I1+2(
    SA = SA*K1*X3/K1S
    SAP = SA*(K1+2)/X
    K2S = K2*(I2+1(*(I2+2(
    SB = SB*K2*X3/K2S
    SBP = SB*(K2+2)/X
    F = F+SA; G = G+SB; FP = FP+SAP; GP = GP+SBP
    IF(ABS(SA( .LT. CONV( .AND. ABS(SB( .LT. CONV( GO TO 200
100 CONTINUE
    OUTPUT ' A FUNCTION DIVERGE'
    OUTPUT I,SA,SAP,SB,SBP
200 AI = C1*F - C2*G
    BI = SQRT(3.(*(C1*F + C2*G(
    AIP = C1*FP - C2*GP
    BIP = SQRT(3.(*(C1*FP + C2*GP(
    A = 0.0
    RETURN
    END
    FUNCTION FB(AI,BI,AIP,BIP,(,Y(
    F1(S( = ((-.35707505E-03*S + .34132453E-02(*S + .39051347(
    F2(S( = ((-.12960774E-03*S+.17892303E-02(*S-.85666906E-02(*
   A         +.41338117
    G1(S( = ((-.20109659E-03*S+.27792805E-02(*S-.13270481E-01(*_
   A         +.42114321
    G2(S( = ((.1831924E-03*S-.25293138E-02(*S+.12107217E-01(*S
   A         +.37855038
    Y = -Y
    Z = LOG(Y(
    (F1 = F1(Z(; (F2 = F2(Z(; (G1 = G1(Z(; (G2 = G2(Z
    COSY = COS(Y(; SINY = SIN(Y(
    (P = (*(*.25
    AI = ((F1*COSY + (F2*SINY(; (P
    BI = ((F2*COSY - (F1*SINY(; (P
    AIP = (P*((G1*SINY - (G2*COSY(
    BIP = (P*((G1*COSY + (G2*SINY(
    FB = 0.0
    RETURN
    END
```

Figure D-3d. Comman Functions of Complex Argument and D:Gamma

```
      FUNCTION GAMMA(X,NFY)
      DOUBLE PRECISION A(26)
      COMPLEX X,X2,X3,X4,Y,Z,GAMMA
      DATA A 1.,.577215664901532,-.655878015202538,-.042002635034095Z,
     1       .166538611382291,-.042197734555544Z,-.009621971527877,
     2       .007218943246663,-.001165167591859Z,-.000215241674114Y,
     3       .000128050282388Z,-.201348547807D-4,-.125049348210-5,
     4       .113302723ZD-5,-.205633841TD-6,.611609SD-8,.500200TSD-8,
     5       - .1312746D-9,.1043427D-9,.778230-11,-.369680--11,.510-12,
     6       -.206D-13,-.54D-14,.14D-14,.1D-15
      IF(CABS(X) .GT. 2.) GO TO 200
      NFY = 1
      Y = (0.,0.); Z = (1.,0.)
      DO 100 I = 1,26
      Z = Z*X
      Y = Y + A(I)*Z
  100 CONTINUE
      GAMMA = 1. Y
      RETURN
  200 Y = CEXP(-X)*X**(X-.5)*2.506628274631
      X2 = X*X
      X3 = X2*X
      X4 = X3*X
      Z = 1. + 1. /12.*X + 1. /288.*X2 - 139. /51840.*X3 -
     A    571. /2488320.*X4
      GAMMA = Y*Z
      NFY = 2
      RETURN
      END
```

```
      FUNCTION PSI(Z)
      COMMON /BLOCK2/CHECK,CHECK1,CHECK2,CHECKU
      LOGICAL CHECK,CHECK1,CHECK2,CHECKU
      DIMENSION ETA(42)
      COMPLEX Y,PSI,Z,ZN,X,SUM,SUM2
      DATA ETA/0.0,1.644934066848226,1.202056903159594,1.082323233711138
     A,1.036927755143369,1.017343061984449,1.008349277381922
     B,1.004077356197944,1.002008392826082,1.000994575127818
     C,1.000494188604119,1.000246086553308,1.000122713347578
     D,1.000061248135058,1.000030588236307,1.000015282259408
     D,1.000007637197637
     E,1.000003817293264,1.000001908212716,1.000000953962033
     F,1.000000476932986,1.000000238450502,1.000000119219925
     G,1.000000059608189,1.000000029803503,1.000000014901554
     H,1.000000007450711,1.000000003725334,1.000000001862659
     I,1.000000000931327,1.000000000465662,1.000000000232831
     J,1.000000000116415,1.000000000058207,1.000000000029103
     K,1.000000000014551,1.000000000007275,1.000000000003637
     L,1.000000000001818,1.000000000000909,1.000000000000454
     M,1.000000000000227/
      DATA R,CONV/.5772156649015 3,1.E-15/
      SUM = (0.,0.);ZN = (1.,0.); SIGN = 1.
      DO 10 I = 1,41
      K = I
      ZN = ZN*Z
      X = ETA(I+1)*ZN
      SUM = SUM + X*SIGN
      SIGN = -SIGN
      IF(CABS(X) .GT. 1.E9)  K = I; GO TO 20
   10 CONTINUE
   20 Y = (-1)**K*(Z**(K+1))
      IF(CHECKU) OUTPUT K,SUM,X,Y
      SUM2 = (0.,0.)
      DO 30 I = 1,1000
      X = 1./((I**(K+1))*(I+Z))
      SUM2 = SUM2 + X
      IF(CABS(X) .LT. CONV) GO TO 40
   30 CONTINUE
   40 SUM2 = SUM2*Y
      PSI = -R-1./Z+SUM+SUM2
      IF(CHECKU) OUTPUT SUM2,I,PSI,X
      RETURN
      END
```

Figure D-3e. Subroutine for Computing Airy Function of a Complex Argument

```
!COPY FR ON ME
      SUBROUTINE F(F2,F2P,XBM,NF3,NF4)
      COMMON /BLOCK1/ ALPHA,PHIB,PHIE,E,H,DIN,L
      COMMON  /BLOCK2/ CHECK,CHECK1,CHECK2,CHECKU
      LOGICAL MORE,CHECK,CHECK1,CHECK2,CHECKU
      COMPLEX F2,F2P,F,II,DT,C1,C2
      REAL IN,IN1,IN2,IN3,IN4
      DATA CON/1.E-7/
      NF3 = 0; NF4 = 0; XB = XBM
      Y = ALPHA*SQRT(E+PHIE); Z = 0.0
      G = E -PHIB
      H = (1.E-2 - PHIB**2)/(4.*Y)
      IF(H .LT. 0.0) H = -H; T = -XB
      A1 = -(ALPHA**2*H)**(1./3.)
      ZO = -(1,0)*G*H
      ZB = A1*(XB-G)*H
      ZOA = ABS(ZO); ZBA = ABS(ZB)
      PI = 3.1415926535; PIM = -PI
      PI2 = 2.*PI; PI2M = -PI2
      ETAO = PI2*(ZOA**1.5)
      ETAB = PI2*(ZBA**1.5)
      IF(ZO .LT. 0.0) ETAO = -ETAO
      IF(ZB .LT. 0.0) ETAB = -ETAB
      IF(CHECK) OUTPUT ZO,ZB,ETAO,ETAB
      IF(ABS(ZO) .LT. DIN) AA = FA(A1,B1,AIP,BIP,ZO);NF3=4;GO TO 5
      IF(ZO.LT.-10.)AA = FB(A1,B1,AIP,BIP,ZOA,ETAO);NF3=5;GO TO 50
      IN1 = IN(PIM,ETAO,NF)
      IN2 = IN(PI,ETAO,NF)
      IN3 = IN(PI2,ETAO,NF)
      IN4 = IN(PI2M,ETAO,NF)
      NF3 = NF
      IF(CHECK1) OUTPUT IN1,IN2,IN3,IN4,ETAO
      IF(ZO .LT. 0.0) GO TO 30
      A1 = PI*SQRT(ZOA)*(IN1 - IN2)
      B1 = SQRT(ZOA 3.)*(IN1 + IN2)
      GO TO 40
   30 A1 = PI*SQRT(ZOA *)(IN1 - IN2)
      B1 = SQRT(ZOA 3.)*(IN1 - IN2)
   40 AIP = -ZOA*(IV4     - IV3)/3.
      BIP = ZOA*(IV4     + IV3)/SQRT(3.)
```

```
50 IF(CHECK1) OUTPUT 20,AI,BI,AIP,BIP
   AIP = AIP*A1; BIP = BIP*A1
   DT = (AI*PIP - PI*AIP)
   C1 = ( PIP - II*BI) DT
   C2 = (II*AI - AIP) DT
   IF(ABS(ZB) .LT. DI) AA = FA(AI,BI,AIP,BIP,ZB,NF,4);GO TO 90
   IF(ZB.LT.-10.)AA = FB(AI,BI,AIP,BIP,ZBA,ETAB);NF4=5;GOTO 90
   II1 = II(IIM,ETAB,NF)
   II2 = II(II,ETAB,NF)
   II3 = II(II2,ETAB,NF)
   II4 = II(II2M,ETAB,NF.
   NF4 = NF
   IF CHECK 1) OUTPUT II1,II2,II3,II4,ZB,ETAB
   IF(ZB .LT. 0.0) GO TO 60
   AI = (II*SQRT(ZBA)*(II1 - II2)
   BI = SQRT(ZBA 3.)*(II1 + II2)
   GO TO 80
60 AI = (II*SQRT(ZBA)*(II1 + II2)
   BI = SQRT(ZBA 3.)*(II1 - II2)
80 AIP = ZBA*(II3 - II4) 3.
   BIP = ZBA*(II3 + II4) SQRT(3.)
90 F2 = C1*AI + C2*BI
   F2P = A1*(C1*AIP + C2*BIP)
   IF(CHECK 1) OUTPUT F2,F2P,C1,C2,AI,BI,AIP,BIP
   RETURN
   END
```


U S GOVERNMENT PRINTING OFFICE 1980 740 1